

1 **Estimation of secondary organic aerosol formation parameters for the**
2 **Volatility Basis Set combining thermodenuder, isothermal dilution**
3 **and yield measurements**

4 Petro Uruci^{1,2}, Dontavious Sippial³, Anthoula Drosatou^{1,2}, and Spyros N. Pandis^{1,2}

5 ¹Institute of Chemical Engineering Sciences (FORTH/ICE-HT), 26504, Patras, Greece

6 ²Department of Chemical Engineering, University of Patras, 26500, Patras, Greece

7 ³Department of Chemical Engineering, Carnegie Mellon University, Pittsburgh, USA

8

9 **Abstract**

10 Secondary organic aerosol (SOA) is a major fraction of the total organic aerosol (OA)
11 in the atmosphere. SOA is formed by the partitioning onto pre-existent particles of low
12 vapor pressure products of the oxidation of volatile, intermediate volatility, and
13 semivolatile organic compounds. Oxidation of the precursor molecules results in a
14 myriad of organic products making the detailed analysis of smog chamber experiments
15 difficult and the incorporation of the corresponding results into chemical transport
16 models (CTMs) challenging. The volatility basis set (VBS) is a framework that has
17 been designed to help bridge the gap between laboratory measurements and CTMs. The
18 parametrization of SOA formation for the VBS has been traditionally based on fitting
19 yield measurements of smog chamber experiments. To reduce the uncertainty of this
20 approach, we developed an algorithm to estimate the SOA product volatility
21 distribution, effective vaporization enthalpy, and effective accommodation coefficient
22 combining SOA yield measurements with thermograms (from thermodenuders) and
23 areograms (from isothermal dilution chambers) from different experiments and
24 laboratories. The algorithm is evaluated with “pseudo-data” produced from the
25 simulation of the corresponding processes assuming SOA with known properties and
26 introducing experimental error. One of the novel features of our approach is that the
27 proposed algorithm estimates the uncertainty of the predicted yields for different
28 atmospheric conditions (temperature, SOA concentration levels, etc.). The uncertainty
29 of these predicted yields is significantly smaller than that of the estimated volatility
30 distributions for all conditions tested.

31

32 **1. Introduction**

33 Submicrometer atmospheric particles are of great importance due to their negative
34 effects on public health (Pope and Dockery, 2006; Lim et al., 2012) and their uncertain

35 influence on Earth's climate (IPCC, 2021). Organic aerosol (OA) contributes 20–90 %
36 to the submicron particulate mass (Zhang et al., 2007) and is emitted directly in the
37 atmosphere as primary particles (POA) or formed as secondary organic aerosol (SOA).
38 SOA constitutes a major fraction of the total OA in the atmosphere contributing more
39 than 60 % on average (Kanakidou et al., 2005). SOA is formed by the condensation of
40 low vapor pressure products of the oxidation of volatile (VOCs), intermediate volatility
41 (IVOCs), and semi-volatile organic compounds (SVOCs).

42 Hundreds of mostly unknown products are formed during the oxidation of each
43 SOA precursor making the detailed description of the corresponding reactions and
44 eventual SOA formation extremely challenging. The volatility basis set (VBS) is one
45 approach that has been proposed to simplify the system and to allow the SOA
46 simulation in CTMs. The VBS describes the volatility distribution of OA using a set of
47 surrogate species with effective saturation concentrations that vary by one order of
48 magnitude (Donahue et al., 2006; Stanier et al., 2008). Volatility is one of the most
49 important physical properties of SOA components as it determines to a large extent
50 their gas-particle partitioning (Pankow, 1994a; 1994b). The parametrization of SOA
51 formation for the VBS requires the determination of the yields of each volatility bin
52 (volatility distribution of products) and the corresponding enthalpies of vaporization.

53 The SOA parametrizations for the VBS have been traditionally based on fitting
54 yield measurements (Lane et al., 2008). The major weakness of this approach is that
55 the resulting parametrization is limited to the range of OA concentrations and
56 temperatures of the measurements. In most cases, the concentration range does not
57 include the low concentrations relevant to the atmosphere and usually most of the
58 experiments take place in a relatively narrow temperature range. Pathak et al. (2007a)
59 needed 37 smog chamber experiments at different temperatures (0–45 °C) and
60 atmospherically relevant concentrations to constrain the α -pinene SOA temperature
61 sensitivity.

62 A number of approaches has been used to minimize the number of experiments
63 needed to characterize the temperature dependence of the SOA formation. Stanier et al.
64 (2007) developed an experimental technique with which the temperature-controlled
65 smog chamber could be heated or cooled after the SOA formation moving the system
66 to new equilibrium favoring evaporation or condensation respectively. However,
67 interactions of the SOA with the walls of the system increased the uncertainties of the
68 approach. Stanier et al. (2008) presented an algorithm to fit the smog chamber

69 experiments using several volatility bins. However, the number of experiments needed
70 by the algorithm should cover a wide range of concentrations and temperatures to
71 effectively constrain the stoichiometric mass yields and the effective vaporization
72 enthalpy.

73 In an effort to cover a wider concentration and temperature range,
74 thermodenuder measurements can be used. The thermodenuder (TD) is a common
75 instrument developed to characterize the volatility of atmospheric aerosols by heating
76 them and observing the resulting changes in size, mass, optical properties, etc.
77 (Burtcher et al., 2001; Wehner et al., 2002, 2004; An et al., 2007). TDs consist of a
78 heated tube in which the volatile particle components evaporate followed by a cooling
79 section with activated carbon to avoid vapor recondensation. The mass changes in TDs
80 depend on the initial SOA concentration, the residence time in the heating tube, the
81 vaporization enthalpy, and the mass transfer resistances. The latter are described by the
82 effective accommodation coefficient that has been traditionally used to account for
83 resistances to mass transfer not only at the surface of the particle but also inside the
84 particle. The evaporation rate for most particles is relatively insensitive to its value
85 when this value is around one. A typical way of reporting the TD measurements is by
86 calculating the aerosol mass fraction remaining (MFR) at a given temperature after
87 passing through the TD. The MFRs in a range of TD temperatures constitute the
88 thermogram.

89 In applications in the field (Cappa and Jimenez, 2010; Huffman et al., 2009; Lee
90 et al., 2010; Louvaris et al., 2017a) and in the laboratory (Kalberer et al., 2004;
91 Baltensperger et al., 2005; An et al., 2007; Lee et al., 2011; Cain et al., 2020) the
92 particles do not reach equilibrium with the gas phase inside the TD. Therefore, dynamic
93 aerosol evaporation models (Riipinen et al., 2010; Cappa, 2010; Fuentes and
94 McFiggans, 2012) are needed for the interpretation of TD measurements. Karnezi et al.
95 (2014) used the time-dependent evaporation model of Riipinen et al. (2010) to calculate
96 the OA volatility distribution, vaporization enthalpy, and mass accommodation
97 coefficient from TD measurements. The authors showed that a simple error
98 minimization approach may not be appropriate for such systems as very similar
99 thermograms can be obtained for multiple combinations of different parameters. For
100 this reason, their approach estimates an ensemble of “good” solutions, from which the
101 best estimate and the corresponding uncertainties are derived.

102 Grieshop et al. (2009) suggested the combination of TD and isothermal dilution
103 to constrain the volatility distribution of SOA. Karnezi et al. (2014) proposed an
104 algorithm to include both types of measurements. The authors concluded that the
105 combination of the two types of measurements can better constrain the OA volatility
106 than each set separately. Louvaris et al. (2017b) and Cain et al. (2020) applied this
107 algorithm to cooking OA (COA) and SOA, respectively. Louvaris et al. (2017b) showed
108 that the use of only TD measurements led to overestimation of the SVOC fraction of
109 COA, while the use of TD and isothermal dilution data reduces the uncertainty of the
110 volatility distribution and the effective vaporization enthalpy. Cain et al. (2020)
111 conducted TD and isothermal dilution experiments for α -pinene and cyclohexene
112 ozonolysis SOA. The SOA in these two systems had similar thermograms, but different
113 areograms. When only thermograms were used in the model, the volatility distributions
114 were quite similar. However, the addition of areograms revealed that α -pinene
115 ozonolysis SOA consists mostly of low-volatility organic compounds (LVOCs) and the
116 cyclohexene ozonolysis SOA consists mostly of SVOCs.

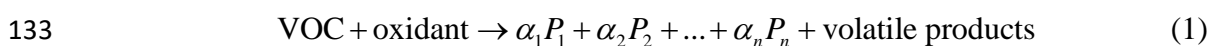
117 To constrain the volatility product distribution of SOA and its effective
118 vaporization enthalpy, we combine TD and isothermal dilution experiments with the
119 SOA yield measurements. We extend here the algorithm of Karnezi et al. (2014) by
120 introducing additional inputs (SOA yields) and by providing additional outputs
121 (uncertainty of estimated yields in relevant atmospheric conditions). The algorithm is
122 tested with “pseudo-experimental” data generated from the use of models simulating
123 the corresponding measurement processes, therefore the true parameters are known.
124 The results of the “pseudo-experiments” are corrupted so that they include experimental
125 errors.

126

127 **2. Model Description**

128 **2.1. SOA Formation**

129 Gas-phase oxidation of VOCs involves a large number of reactions and produces a large
130 number of products that can condense in the particulate phase. Depending on their
131 effective saturation concentration, they can be represented in the 1D-VBS framework
132 by



134 where n is the number of the surrogate compounds (volatility bins in the VBS), P_i is the
 135 surrogate product in the i -th volatility bin and α_i is the corresponding stoichiometric
 136 mass yield. The total SOA mass yield can be then calculated as:

$$137 \quad Y \equiv \frac{C_{\text{OA}}}{\Delta\text{VOC}} = \sum_i^n \frac{\alpha_i}{1 + (C_i^*/C_{\text{OA}})} \quad (2)$$

138 where C_{OA} is the total SOA concentration, ΔVOC is the consumed concentration of the
 139 VOC and C_i^* is the effective saturation concentration of compound i . This yield
 140 equation is an extension of the two-product model by Odum et al. (1996) replacing their
 141 semi-empirical partitioning coefficients with the assumption of a pseudo-ideal solution
 142 (Strader et al., 1999). This model assumes that the system has reached equilibrium when
 143 the yield was measured and that the differences in molecular weights are small.

144 The effective saturation concentrations at different temperatures are given by
 145 the Clausius-Clapeyron equation:

$$146 \quad C_i^*(T) = C_i^*(T_{\text{ref}}) \frac{T_{\text{ref}}}{T} \exp \left[\frac{\Delta H_{\text{vap},i}}{R} \left(\frac{1}{T_{\text{ref}}} - \frac{1}{T} \right) \right] \quad (3)$$

147 where T_{ref} is the reference temperature in which the reference effective saturation
 148 concentration is defined (298 K in this work), and $\Delta H_{\text{vap},i}$ is the enthalpy of vaporization
 149 of surrogate compound i .

150

151 2.2. Thermodynamic Model

152 The time-dependent evaporation of SOA in the TD used in this work is described by
 153 the dynamic mass transfer model of Riipinen et al. (2010). The evolution of the total
 154 particle mass, m_p , and the gas phase concentration of the compound i , C_i are given by:

$$155 \quad \frac{dm_p}{dt} = - \sum_{i=1}^n I_i \quad (4)$$

$$156 \quad \frac{dC_i}{dt} = I_i N_{\text{tot}} \quad (5)$$

157 where n is the number of surrogate compounds, N_{tot} is the total number concentration
 158 of particles (assuming monodisperse aerosol population) and I_i is the mass flux of
 159 compound i from the gas to the particulate phase for each particle calculated by
 160 (Seinfeld and Pandis, 2016):

$$161 \quad I_i = \frac{2\pi d_p M_i \beta_{mi} D_i}{RT_{\text{TD}}} (p_i - p_i^0) \quad (6)$$

162 where d_p is the particle diameter, R is the ideal gas constant, M_i is the molecular weight
 163 of compound i , D_i is the diffusion coefficient of compound i in the gas phase at
 164 temperature T_{TD} , p_i and p_i^0 are the partial vapor pressures of i far away from the particle
 165 and at particle surface, respectively, and β_{mi} is a factor for the correction of kinetic and
 166 transition regime effects (Fuchs and Sutugin, 1970):

$$167 \quad \beta_{mi} = \frac{1 + Kn_i}{1 + \left(\frac{4}{3\alpha_{mi}} + 0.377 \right) Kn_i + \frac{4}{3\alpha_{mi}} Kn_i} \quad (7)$$

168 where Kn_i is the Knudsen number of compound i , and α_{mi} is the mass accommodation
 169 coefficient of compound i on the particles. The partial vapor pressure of compound i at
 170 the particle surface is given by:

$$171 \quad p_i^0 = x_{mi} \frac{C_i^* RT}{M_i} \exp\left(\frac{4M_i \sigma}{RT_{TD} \rho d_p} \right) \quad (8)$$

172 where x_{mi} is the mass fraction of compound i in the particulate phase, C_i^* is the effective
 173 saturation concentration, σ is the surface tension (assumed 0.05 N m^{-1} in our
 174 simulations), T_{TD} is the particle temperature assumed to be the same as in the TD, and
 175 ρ is the particle density. The effective saturation concentrations at different TD
 176 temperatures are given by Eq. (3).

177 Processes other than organic aerosol evaporation may affect the TD
 178 measurements. For example, thermal decomposition may accelerate the transfer of
 179 organic compounds from the particulate to the gas phase and may lead to overestimation
 180 of the volatility of especially the least volatile components of the SOA (Epstein et al.,
 181 2010; Saha and Grieshop, 2016; Stark et al., 2017). However, the corresponding
 182 parameters for the SVOCs and the more volatile LVOCs that are important for
 183 atmospheric SOA modeling should be a lot less uncertain given that they are measured
 184 in relatively low TD temperatures. The use of isothermal dilution measurements may
 185 also help identify cases in which the model does not include a process (e.g., thermal
 186 decomposition) that dominates the behavior of the aerosol during heating. In this case,
 187 one expects that the overall algorithm will have difficulties reproducing all
 188 measurements (yields, isothermal dilution, and evaporation in the TD).

189

190 **2.3. Isothermal Dilution Model**

191 In isothermal dilution experiments, a SOA sample is injected in a reactor filled with
192 clean air at room temperature. The concentrations of both the gas and particulate phase
193 components are lowered due to dilution leading the system out of equilibrium. The
194 evaporation of SOA as a result of isothermal dilution is also described by equations (3)-
195 (8) (Karnezi et al., 2014), but the temperature is equal to 298 K. Evaporation in a
196 dilution chamber depends on the initial SOA mass, time, and the α_m , but not on ΔH_{vap}
197 as the particles evaporate without a change in temperature.

198 The dilution ratio is an important parameter, varying typically from 10 to 20 in
199 SOA experiments (Cain et al., 2020). Low dilution ratios result in little evaporation and
200 little signal to be explored by the parameter estimation algorithm. High dilution ratios
201 lead to very low initial concentrations in the dilution chamber and a lot of noise in the
202 subsequent evaporation measurements.

203

204 **3. Algorithm for the Estimation of VBS Parameters**

205 The algorithm of Karnezi et al. (2014) was first extended to include an SOA partitioning
206 model described by Equations (1) – (3) together with the TD and isothermal dilution
207 models in order to estimate the volatility product distribution, vaporization enthalpy
208 and accommodation coefficient. We discretized the domain of the parameters and
209 simulated all combinations of stoichiometric mass yields (α_i), ΔH_{vap} , and α_m . The yields
210 α_i were allowed to vary from 0.0 to 0.8, with values of 0.0, 0.05, 0.1, 0.15, 0.2, 0.3, 0.4,
211 0.6, and 0.8. The user of the algorithm can specify an upper limit for the sum of the
212 yields to reduce the number of the potential solutions that the algorithm will test.
213 Combinations with sum of the yields exceeding 1.0 were excluded from the analysis
214 originally. The sensitivity of our results to setting the upper limit of the sum of the
215 yields equal to 2 is examined in Section 4.6. For a 4-product system there are 3,153 and
216 for 6-product system 66,636 acceptable combinations. The values used for ΔH_{vap} were
217 from 20 to 200 kJ mol⁻¹ with a step of 20, and for α_m , the values used were 0.001, 0.01,
218 0.1, and 1. As a result 126,120 simulations are needed (computational time of about 15
219 h in an office PC) for a 4-product VBS and 2,665,440 for a 6-product solution.

220 For each simulation and each type of measurement, we calculated the
221 *normalized mean square error* (NMSE) defined as

222

$$\text{NMSE} = \frac{\sum_{i=1}^{N_O} (P_i - O_i)^2}{\sum_{i=1}^{N_O} O_i} \quad (9)$$

223 where O_i represents the i th observed value (corresponding to a specific SOA
 224 concentration for yield measurements or temperature for TD, or time for isothermal
 225 dilution), P_i the corresponding model-predicted value, and N_O is the total number of
 226 observations from each type of measurement. For each simulation (denoted as s), the
 227 overall error was calculated by assuming equal weight to the set of yield, TD, and
 228 dilution measurements and summing the corresponding errors:

229

$$E_s = \text{NMSE}_{Y,s} + \text{NMSE}_{\text{TD},s} + \text{NMSE}_{\text{Dil},s} \quad (10)$$

230

The parameter combinations for which the overall error E_s is less than 5% are
 231 identified. The best solution is then calculated by averaging these solutions using the
 232 inverse error E_s as a weighting factor. The solutions that are closer to the measurements
 233 have higher weight. Therefore, for every combination of α_i , ΔH_{vap} , and α_m the algorithm
 234 calculates one overall NMSE following Eq. (10) and all data points for each solution
 235 get the same weighting factor. More specifically the best estimate \bar{x} is given by:

236

$$\bar{x} = \frac{\sum_k^N x_k \frac{1}{E_k}}{\sum_k^N \frac{1}{E_k}} \quad (11)$$

237

where x_k is the estimated value of a property (mass yield of a volatility bin, effective
 238 vaporization enthalpy, or effective accommodation coefficient) and N is the number of
 239 combinations with error below the threshold value. The uncertainty range of the
 240 parameters is estimated by calculating the standard deviation (σ):

241

$$\sigma = \sqrt{\frac{\sum_k^N \left[(x_k - \bar{x})^2 \cdot \frac{1}{E_k} \right]}{\sum_k^N \frac{1}{E_k}}} \quad (12)$$

242 following Karnezi et al. (2014).

243

244 4. Testing of the Algorithm

245 4.1. Generation of Data for Evaluation

246 In order to evaluate the algorithm, we generated data using the output of SOA
247 formation, thermodenuder and isothermal dilution models described in Section 2 for
248 systems with known volatility distribution of the products, and properties. Then, these
249 data were “corrupted” with random errors to represent the “noise” observed in
250 laboratory measurements for yields, thermograms, and areograms. As a result, there is
251 no set of model parameters that can reproduce all the “measurements”. The yields were
252 corrupted based on the variability of laboratory measurements of Pathak et al. (2007a),
253 by assuming a normal distribution and standard deviation (σ_Y) given by:

$$254 \quad \sigma_Y = 0.1 Y_{\text{true}} + 0.02 \quad (13)$$

255 where Y_{true} are the correct yields.

256 For TD, the errors were calculated by assuming a normal distribution and the
257 standard deviation (σ_{TD}) suggested by Karnezi et al. (2014):

$$258 \quad \sigma_{\text{TD}} = 0.51 MFR_{\text{TD,true}} - 0.5 (MFR_{\text{TD,true}})^2 \quad (14)$$

259 where $MFR_{\text{TD,true}}$ are the correct MFR values for each TD temperature.

260 For dilution, the errors were calculated by assuming a uniform distribution and
261 standard deviation (σ_{Dil}) suggested by Karnezi et al. (2014):

$$262 \quad \sigma_{\text{Dil}} = 0.05 MFR_{\text{Dil,true}} + 0.03 \quad (15)$$

263 where $MFR_{\text{Dil,true}}$ are the correct MFR values for isothermal dilution.

264 Based on the above methodology, we generated “pseudo-measurements” of
265 yield, TD, and isothermal dilution for different SOA systems. The parameters used to
266 produce the pseudo-experimental data are summarized in Table S1. The “experimental”
267 conditions assumed for the TD and isothermal dilution measurements are shown in
268 Table S2.

269 In “Experiment” A, we test the performance of the algorithm against α -pinene
270 ozonolysis data and examine the effect of TD and isothermal dilution data. For
271 “Experiment” A, the “true” values were taken from the parameterization derived by
272 Pathak et al. (2007b) for the ozonolysis of α -pinene at low NO_x , dark and low RH
273 conditions. Therefore, these results are good fits of the measurements analyzed in that
274 study. The parametrization was derived assuming a 4-volatility bin system with
275 saturation concentrations ranging from 1 to $10^3 \mu\text{g m}^{-3}$. The effective vaporization
276 enthalpy estimated in that study was equal to 30 kJ mol^{-1} . Because the effective

277 accommodation coefficient was not part of the Pathak et al. (2007b) parametrization,
278 we assumed a value of 0.5 in this work. We used a small number of yield measurements
279 at atmospherically relevant SOA concentrations of 1, 5, 10, 20 and 40 $\mu\text{g m}^{-3}$ (Fig. 1).
280 For this SOA system, the yield at 40 $\mu\text{g m}^{-3}$ did not exceed 20%. The thermogram
281 includes ten MFR data points in the temperature range of 20 to 200 °C. For the highest
282 temperature, more than 70% of the SOA mass was evaporated. The areogram shows
283 that the correspondent SOA evaporated almost by 70 % in the first 0.5 h and more than
284 90% in less than 3 h.

285 For “Experiment” B, the “true” values were taken from the alternative
286 parametrization proposed by Pathak et al. (2007b) for the same oxidation system as
287 described before. This time, the authors used a 7-volatility bin system with saturation
288 concentrations ranging from 10^{-2} to 10^4 $\mu\text{g m}^{-3}$ in their parametrization. The effective
289 vaporization enthalpy of the parametrization was 30 kJ mol^{-1} , while for the
290 accommodation coefficient we assumed again a value of 0.5. The yield, TD and
291 isothermal dilution “measurements” of Experiment B are generated in the same SOA
292 mass concentration, temperature, and dilution time range as in the previous pseudo-
293 experiment (Fig. 2).

294 For “Experiment” C, the “true” values were based on the parameterization of
295 the SOA formed during α -humulene ozonolysis by Sippial et al. (2022). The authors
296 measured high SOA yields for α -humulene in the main smog chamber (~70% at 60 μg
297 m^{-3}), and their corresponding thermogram suggested that the SOA particles fully
298 evaporated at 150 °C, while the areogram showed modest (20%) evaporation in the
299 dilution chamber after 3 hours. A 4-volatility bin set with saturation concentrations
300 ranging from 10^{-2} to 10 $\mu\text{g m}^{-3}$ was used in that study to fit the measurements. The
301 stoichiometric coefficients of the three least volatile bins (10^{-2} , 10^{-1} and 1 $\mu\text{g m}^{-3}$) were
302 around 0.1 and for the most volatile (10 $\mu\text{g m}^{-3}$) 0.25. The vaporization enthalpy was
303 115 kJ mol^{-1} and the accommodation coefficient was 0.01 (Table S1). We assumed five
304 yield “measurements” in the SOA concentration range of 1 to 100 $\mu\text{g m}^{-3}$ with yield
305 values as high as 65 % at 100 $\mu\text{g m}^{-3}$ (Fig. 3). The corresponding thermogram consisted
306 of 10 data and the particles fully evaporated at TD temperatures higher than 150 °C.
307 The areogram consisted of 17 data points and only 20 % of the SOA evaporated in the
308 dilution chamber.

309

310 4.2. Parameter Estimation for “Experiments” A, B, and C

311 We explored the performance of the algorithm for different choices of the number of
312 volatility bins, the range of saturation concentrations, and the range of SOA mass
313 concentration range in the yield measurements. For each test, the “true” and the
314 estimated properties are summarized in Table 1.

315 We evaluated the performance of our parameter estimation algorithm
316 comparing its predictions both against the “measurements” and the “truth” defined as
317 the predictions of the original parameterization. In both comparisons, *mean normalized*
318 *error* (MNE) (Emery et al., 2017) was used as the evaluation metric because it has a
319 simpler physical meaning than NMSE.

320 For the evaluation against the “measurements”, the MNE_M was defined as

$$321 \quad MNE_M = \frac{100}{N_o} \sum_{i=1}^{N_o} \frac{|EST_i - O_i|}{O_i} \quad (16)$$

322 where EST_i is the estimated by the algorithm value and corresponds to a specific
323 measured point O_i .

324 For the evaluation against the “truth”, which includes conditions (e.g.,
325 temperatures or concentrations) for which there are no available measurements, the
326 MNE_T was defined as:

$$327 \quad MNE_T = \frac{100}{N_d} \sum_{j=1}^{N_d} \frac{|EST_j - TR_j|}{TR_j} \quad (17)$$

328 where EST and TR are the estimated and the “true” values respectively. N_d is the total
329 number of data points included in calculations and depends on the selected
330 discretization of the corresponding dependent variable (e.g., SOA concentration, TD
331 temperature, and dilution time). We used a linear discretization for the SOA
332 concentrations (from 0.01 to 50 $\mu\text{g m}^{-3}$ with a step of 0.01) and the TD temperatures
333 (20 to 200 $^{\circ}\text{C}$ with a step of 5 $^{\circ}\text{C}$ but excluding zero MFR values to avoid the division
334 by zero). For the dilution time, the sampling time step was not constant. We used a
335 higher resolution for the first 0.5 hour (step of 2 min), in which the evaporation is
336 usually faster, and a lower resolution afterwards (step of 10 min).

337 Finally, we used the average relative standard deviation ($ARSD$) as a metric to
338 quantify the uncertainty of the estimates (range of good solutions) using the same
339 discretization as in the MNE_T metric. The $ARSD$ is given by:

340
$$ARSD = \frac{100}{N_d} \sum_{j=1}^{N_d} \frac{\sigma_j}{EST_j} \quad (18)$$

341 where σ_j is the standard deviation for data point j .

342

343 4.2.1 Parameter Estimation for “Experiment” A

344 In Test A1, we applied the algorithm in the same range of saturation concentrations and
 345 with the same number of volatility bins as these used to produce the “experimental”
 346 data. The upper bin ($10^3 \mu\text{g m}^{-3}$) exceeded the maximum SOA concentration ($40 \mu\text{g}$
 347 m^{-3}) in the measurement range by one order of magnitude.

348 Figure 1 depicts the estimated and the range of the ensemble of best solutions
 349 for the three types of “measurements” for Test A1. There were 148 “good” solutions
 350 under the 5% threshold out of the 126,120 simulations (Table S3). The density
 351 distribution of the solutions is depicted in Figure S1. The performance of the model for
 352 the yields at 25 °C was quite encouraging with a small tendency of overprediction for
 353 SOA higher than $10 \mu\text{g m}^{-3}$. The MNE_M of the model for the SOA yield “measurements”
 354 (given by Eq. 16) was equal to 25% (Table 2). The corresponding discrepancy between
 355 the true parameterization and the measurements (due to the measurement error that we
 356 introduced) was 21.2% (Table 2). This indicates that a significant part of the algorithm
 357 error can be explained by the uncertainty introduced in the measurements.

358 Our algorithm can be used to calculate the SOA yield at different concentrations
 359 and temperatures. The yields were calculated in the atmospherically relevant range of
 360 $0\text{--}50 \mu\text{g m}^{-3}$ SOA concentration and at four temperatures (5, 15, 25, and 35 °C) using
 361 the true parameter values and the estimated parameters of Test A1 (Fig. 1a-d). At 25 °C
 362 (Fig. 1c), the estimated yield curve is in good agreement with the “true” yield curve for
 363 SOA concentrations lower than $6 \mu\text{g m}^{-3}$ (error of 8% at $6 \mu\text{g m}^{-3}$), but the discrepancies
 364 increase at higher concentrations (error of 23% at $50 \mu\text{g m}^{-3}$). The average MNE_T error
 365 between the true parametrization and the estimated values (given by Eq. 17) was equal
 366 to 17.3% for yields at 25 °C (Table 3). The uncertainties, as expected, are larger at lower
 367 temperatures. However, the MNE_T error (estimated yields compared to the true value)
 368 remains less than 25% (Table 3) even at 5 °C, quite far from the measurement
 369 temperature. Both MNE_T and MNE_M were quite close to the introduced experimental
 370 error. Their difference can be explained by both the “noise” introduced to the

371 “measurements” that affects MNE_M and the higher number of points used to calculate
372 MNE_T .

373 The SOA model used in this work assumes that the stoichiometric coefficients
374 (α_i) are temperature independent. Therefore, processes, such as formation of highly
375 oxygenated organic molecules (HOMs) and oligomerization which are expected to be
376 temperature dependent (Quéléver et al., 2019; Gao et al., 2022), are not described by
377 our algorithm.

378 The algorithm provides a range of “good” estimates in addition to the best
379 estimate. The range can be defined by the lower and upper SOA yield limits of the
380 ensemble of the good solutions at each point. At 25 °C, the yield range increased, as
381 expected, at higher concentrations (yield range of 0.05 at 1 $\mu\text{g m}^{-3}$ to 0.17 at 50 μg
382 m^{-3}). The average relative standard deviation ($ARSD$ of the estimated yields defined by
383 Eq. 18) was equal to 26% (Table 4) for the 25 °C case. For the rest of the temperatures,
384 the $ARSD$ increased for the lower temperatures, ranging from 24% at 35 °C to 35% at
385 5 °C (Table 4) and including in all cases the true solution.

386 For the TD (Fig. 1e), the model reproduced well the correspondent thermogram
387 with low errors compared to the “measurements” with an error MNE_M of 7% (Table 2).
388 The error MNE_T compared to the “true” values was 5.5% (Table 3). The error of the
389 TD “measurements” compared to the true values was equal to 7.6% (Table 2).
390 Therefore, the error of the proposed algorithm is quite similar to the experimental error.
391 The error introduced into the “measurements” was transferred, as expected, to the error
392 metrics of the algorithm.

393 For the isothermal dilution (Fig. 1f), the algorithm did reasonably well for the
394 first 30 minutes and then the evaporation was slightly underpredicted leading to an error
395 MNE_M of 16.7% (Table 2). This MNE_M value was roughly two times higher than the
396 corresponding error between the dilution measurements and the true parametrization
397 (Table 2). The error between the estimated and the “true” values MNE_T was 19%. The
398 $ARSD$ of 24% (Table 4) was sufficient to include the true solution.

399 The estimated volatility distribution of the products and the effective
400 vaporization enthalpy and accommodation coefficient using the three types of
401 measurements can be seen in Figure 4 and Table 1. The estimated volatility distribution
402 of the products was in a good agreement with the “true” values (α_i absolute difference
403 of 0.01 at 1 $\mu\text{g m}^{-3}$, 0.03 at 10 $\mu\text{g m}^{-3}$, 0.07 at 10² $\mu\text{g m}^{-3}$, and 0.04 at 10³ $\mu\text{g m}^{-3}$) and
404 the estimated uncertainties contained the correct values. There is a large uncertainty

405 range for the two higher volatility bins (standard deviation higher than 0.13) indicating
406 that yield values at higher SOA concentrations would be needed to better constrain
407 these volatility bins. The relative error of the estimated ΔH_{vap} is 10%. The estimated
408 accommodation coefficient was 0.17 compared to a true value of 0.5. The estimated
409 uncertainty for the effective accommodation was almost one order of magnitude (from
410 0.06 to 0.51) indicating the difficulty of constraining this parameter when it is close to
411 unity and thus the resistances to mass transfer are small.

412

413 **4.2.2 Parameter Estimation for “Experiment” B**

414 In this section, we analyze the pseudo-experimental data of Experiment B, which were
415 obtained from the parametrization of the same smog chamber results used in
416 Experiment A, but with more components and a much wider range of volatilities
417 including LVOCs, SVOCs and IVOCs (10^{-2} – 10^4 $\mu\text{g m}^{-3}$). In Test B1, the algorithm was
418 applied using a 4-bin VBS with saturation concentrations ranging from 1 to 10^3 $\mu\text{g m}^{-3}$
419 m^{-3} . In this test, we attempted to model the behavior of the system with a narrower
420 volatility range than the real one. The upper limit of the saturation concentration range
421 that we tested did not exceed the 10^3 $\mu\text{g m}^{-3}$ because Experiment B took place in
422 moderate SOA concentration levels (up to 40 $\mu\text{g m}^{-3}$), which means that it is practically
423 impossible to constrain the 10^4 $\mu\text{g m}^{-3}$ or higher volatile bins. Figure 2 shows the results
424 of the fitting for the three types of “measurements” in this experiment. There were 82
425 “good” solutions under the 5% threshold out of 126,120 simulations (Table S3) and the
426 density of the solutions are shown in Figure S2. At 25 °C, the model performance for
427 the yields is encouraging ($MNE_M=20.6\%$). This is again pretty close to the measurement
428 error (20.5%). By comparing the estimated and the “true” yield curves at 25 °C, the
429 error MNE_T is now 14%. The error increases to 31% at 5 °C, far from the available
430 measurements. This is reflected also in the increase of the uncertainty of our estimates
431 with the $ARSD$ increasing from 17% at 35 °C to 37% at 5 °C (Table 4). Once more the
432 uncertainty range estimated by the algorithm includes the true values.

433 Both “measured” and “true” thermogram were well captured by the best
434 estimate (MNE_M of 6% and MNE_T of 4%) with an uncertainty $ARSD$ of 20.5%. The
435 evaporation in the dilution chamber was a little underestimated for the first 2 h, but then
436 it was slightly overpredicted. The MNE_T for the areogram was 13.3% and the true values
437 were included within the range of the estimates ($ARSD$ of 18%).

438 Figure 5 shows the results of Test B1 for the volatility distribution of the
439 products. The “true” stoichiometric coefficient for the $1 \mu\text{g m}^{-3}$ bin was overestimated
440 by 0.01 by the algorithm. This overestimation actually corresponds to the total material
441 of the 10^{-2} and $10^{-1} \mu\text{g m}^{-3}$ bins of the “true” system. This indicates that the algorithm
442 places the material of the two lowest bins that are not part of the solution to the bin with
443 the lower volatility. For the $10 \mu\text{g m}^{-3}$ and $10^2 \mu\text{g m}^{-3}$ bins, the relative errors between
444 the estimated and “true” were 58% and 277% respectively (Table S4), while for the 10^3
445 $\mu\text{g m}^{-3}$ bin, the relative error was 10 %. The ΔH_{vap} was predicted accurately (error of
446 only 4%), while α_m was underpredicted (0.1 instead of 0.5). The model compensates
447 for the missing volatility bins by increasing the material in the $10^2 \mu\text{g m}^{-3}$ bin and by
448 decreasing the accommodation coefficient.

449 The results of Test B1 suggest that the mismatch between the actual SOA
450 volatility distribution and the range used for the fits can introduce significant errors in
451 the retrieved distribution for individual volatility bins. However, despite these
452 problems, the yields predicted by the derived parameterizations have a much lower
453 error than the volatility distribution. This is a valuable insight for the strengths and
454 weaknesses of this and other similar SOA parameter estimation algorithms.

455

456 4.2.3 Parameter Estimation for “Experiment” C

457 In Test C1, we obtained the best fits for the pseudo-measurements of Experiment C by
458 applying the algorithm in the same range of saturation concentrations and with the same
459 number of volatility bins (4 volatility bins in the 10^{-2} – $10^1 \mu\text{g m}^{-3}$ saturation
460 concentration range) as the true volatility distribution.

461 Figure 3 shows the results of the fitting for the three types of “measurements”.
462 There were 3,479 “good” solutions under the 5% threshold out of the 126,120
463 simulations (Table S3). The density distribution of the solutions is shown in Figure S3.
464 The best estimate for the SOA yields at 25 °C was in a good agreement with the
465 “measurements” ($MNE_M=6.3\%$) and the “true” values ($MNE_T=9.6\%$). For the rest of
466 the temperatures, there was a decreasing trend of the error as the temperature decreased
467 varying from 15.5% at 35 °C to 6.2% at 5 °C. A similar decreasing trend was observed
468 for the uncertainty $ARSD$ of the estimates which varied from 23% at 35 °C to 15% at 5
469 °C. This behavior is the opposite from what we observed in the previous tests, in which
470 both errors and uncertainties increased at lower temperatures. However, the changes in
471 both the error and the uncertainty are small (change of around 7% between the upper

472 and lower temperature for both metrics), indicating that this system is less temperature-
473 sensitive in this temperature range than the previous ones.

474 The performance of the algorithm was satisfactory compared to the TD
475 “measurements” ($MNE_M=12.9\%$). The corresponding error of the algorithm for the true
476 values (MNE_T) was 4.4% for temperatures up to 110 °C and equal to 10.6% for the
477 lower values at higher temperatures. According to Figure 3, the evaporation due to
478 dilution was initially overestimated for the first 30 min, but then underestimated
479 (highest MFR discrepancy of 0.05) and there is a high uncertainty range of the
480 corresponding estimates (MFR range of 0.46 at 3 h). However, the low dilution values
481 resulted in low relative errors (MNE_M of 3.5% and MNE_T of 2.7%).

482 Figure 6 shows that the highest relative errors were calculated for the 10^{-1} and
483 $10^0 \mu\text{g m}^{-3}$ bins (23% and 33% respectively), and smaller relative errors for the other
484 two bins (less than 13%). The uncertainties were almost of the same magnitude for all
485 bins with standard deviations ranging from 0.09 to 0.13. The performance of the model
486 was good for the ΔH_{vap} (relative error of 7%), but with high uncertainty for α_m .

487

488 **4.3. Effect of the Volatility Range**

489 In in this section, we explore the performance of the algorithm for different choices of
490 the number of volatility bins and the range of saturation concentrations. The analysis
491 of the results of Test B1 has already quantified the effects of using a narrower volatility
492 distribution in the parameter estimation algorithm than the one of the investigated SOA
493 system. Additional sensitivity tests are performed here for all cases.

494 In Test A2, we used 3 volatility bins covering the $1\text{--}10^2 \mu\text{g m}^{-3}$ saturation
495 concentration range instead of the 4 bins used in Test A1. The narrower assumed
496 volatility range had a very small effect on the estimated yields at all temperatures (Table
497 3 and Fig. S4) compared to Test A1. The change in MNE_T ranged from 3% at 5 °C to
498 0.3% at 35 °C. Minor changes were detected in the predicted thermogram (change of
499 0.8%) and areogram (change of 0.5%) as well. The uncertainty of the yield estimates
500 increased by less than 2.5% at all temperatures. The estimated volatility distribution of
501 the SOA products of Test A2 changed by less than 5% in the two lower bins. The
502 material in the $10^2 \mu\text{g m}^{-3}$ increased by 15% to account for the SOA of higher volatility
503 that could not be included otherwise in the estimated distribution. The estimated ΔH_{vap}
504 was in this case 32 kJ mol^{-1} (2.7% decrease) and the α_m decreased by 12% with respect
505 to Test A1.

506 In Test A3, we shifted the assumed 4-bin volatility distribution by one order of
507 magnitude to lower values (from 1–1000 $\mu\text{g m}^{-3}$ in Test A1 to 0.1–100 $\mu\text{g m}^{-3}$ in Test
508 A3). In this case, the algorithm distributed exactly the same material to the 1, 10 and
509 100 $\mu\text{g m}^{-3}$ volatility bins as in Test A2, and it predicted correctly zero SOA in the 0.1
510 $\mu\text{g m}^{-3}$ bin (Table 1). The ΔH_{vap} and α_{m} estimated values were also unchanged with
511 respect to Test A2. This in turn, led to the same estimated yields at different
512 temperatures (no change in the error between the two tests).

513 In Test C2, we applied the algorithm against the Experiment C “measurements”
514 using a 4-volatility bin system in the 1 to $10^3 \mu\text{g m}^{-3}$ range, that is two orders of
515 magnitude higher than the actual range of the “true” values. Figure 7 shows the results
516 of the fitting for the three types of “measurements”. Despite the significant mismatch
517 of the volatility distributions the MNE_{M} increased by only 2.3% for the estimated SOA
518 yields. The error for the TD measurements increased by 20% while it actually decreased
519 a little (1.2%) for the dilution data. The errors compared to the true values increased by
520 less than 3% for the temperature range 15–35 °C while it increased by 12% at 5 °C.
521 These results suggest that the estimated yields are quite robust in this case to the
522 assumed volatility range. The major effect of the mismatch in volatility ranges was
523 evident in the predicted thermogram with overestimation of the MFR for the 60–120
524 °C temperature range and underprediction in higher temperatures. The increase in
525 MNE_{T} for the TD MFR was 17.2% (Table 3). The change in the predicted areogram
526 was marginal and led to a small increase of MNE_{T} (error increase by 0.7%) (Table 3).
527 The algorithm underestimated again the α_{m} (0.004 instead of 0.01) but also recognized
528 the high uncertainty of the corresponding estimate. The algorithm distributed
529 significant material to the 1 $\mu\text{g m}^{-3}$ bin (3.6 times higher than the actual), in an effort to
530 account for the absence of the 10^{-2} and $10^{-1} \mu\text{g m}^{-3}$ bins. The ΔH_{vap} was underestimated
531 with an error of 21%.

532 The results of the above tests indicate that a mismatch between the true and
533 assumed volatility ranges of the SOA increases in general the estimation error but the
534 increase is small to modest. This is reassuring for the robustness of the proposed
535 algorithm.

536

537 **4.4. Effect of Measurements at High SOA Levels**

538 During the last decade there has been a significant shift of the performed SOA smog
539 chamber towards lower SOA concentrations. This is needed to increase the accuracy at

540 the ambient concentration levels. The high SOA concentration experiments that once
541 represented the majority of the performed experiments are becoming increasingly rare.
542 In this paragraph we examine the value of these high concentration experiments for the
543 estimation of SOA yields at ambient conditions.

544 To examine the effect of “measurements” at SOA levels much higher than the
545 atmospheric ones, we included an extra yield measurement at $200 \mu\text{g m}^{-3}$ in the yield
546 data of Experiments A and B. In Test A4 and B2, we applied the algorithm once again
547 against the three types of “measurements” by using a 4-volatility bin system with
548 saturation concentrations ranging from 1 to $10^3 \mu\text{g m}^{-3}$.

549 In Test A4, the additional experiment at high SOA concentration led to an MNE_T
550 of 15.7% for the yields at 25°C (Table 3 and Fig. S5), which is by 1.6% lower than that
551 without this experiment in Test A1. The improvement was more significant at lower
552 temperatures e.g., the MNE_T at 5°C was reduced from 24.4% to 20.4%. The reduction
553 in the $ARSD$ for the SOA yields ranged from 3.8% at 5°C to 0.9% at 35°C (Table 4).
554 Figure 8 depicts the results of the model for the yields and the volatility distribution of
555 the products for Test A4. The accuracy of the predicted volatility distribution increased
556 especially for the higher volatility material. For example, the error for the $10^2 \mu\text{g m}^{-3}$
557 bin was reduced from 41% in Test A1 to 6% in this case (Table S3). Minor changes in
558 the errors were detected for the ΔH_{vap} and α_m between the two tests (3% increase and
559 6% decrease respectively).

560 Similar to Test A4, in Test B2 we added a yield measurement at $200 \mu\text{g m}^{-3}$ in
561 the Experiment B set of “measurements”. Figure 9 depicts the results of the model for
562 the SOA yields at 25°C and the estimated volatility distribution of the products. The
563 use of the additional data point led to a reduction of the NME_T from 13.9% in Test B1
564 to 9% in Test B2 at 25°C (Table 3). Similar reductions in the NME_T were observed for
565 the other temperatures, with the highest one observed at 5°C (lower error by 7%)
566 (Figure 10). The reduction in the $ARSD$ for the estimated yields ranged from 3.3% at 5°C
567 to 1.2% at 35°C (Table 4). Minor changes were observed for the estimated
568 thermogram (Fig. S6) (change in the NME_T of 1.5%) and the uncertainty of the
569 estimates (change in the $ARSD$ of 2.5%). The error in the estimated areogram was also
570 small but in this case the error increased by 5%. The additional data point helped
571 decrease the errors for the estimated mass of the more volatile SOA products (Fig. 9)
572 and especially for the $10^2 \mu\text{g m}^{-3}$ bin. The ΔH_{vap} and α_m estimated values were only
573 slightly affected by the additional measurement.

574 By comparing the results Tests B1 and B2 with Case A, one would expect that
575 the retrieved volatility distribution of the products will be quite similar. The differences
576 present are due to a large extent to the different random experimental errors introduced
577 in the two sets of “measurements” for Experiments A and B. A second reason for the
578 differences is that parametrizations of the two “Experiments” by Pathak et al. (2007b)
579 even if they were derived from the same smog chamber experiments have some
580 differences. As a result, the “true” yields, thermogram, and areogram in Cases A and B
581 are not exactly the same (Figs. 1 and 2).

582 These results suggest that an additional yield measurement at high SOA can
583 lead to a substantial reduction of the error for the estimated yields at low temperatures
584 (Fig. 10) and also a better estimation of the SOA products with higher volatility (10^2
585 and $10^3 \mu\text{g m}^{-3}$). These products may contribute little to the SOA concentration at 25
586 °C, but their reactions (aging) could lead to significant additional SOA in later stages.

587

588 **4.5. Significance of Each Type of Measurement for the Parametrization**

589 To quantify the effect of each type of measurement for the parameter estimation and
590 their subsequent effect on the estimated SOA yields, we repeated tests A1, B1, and C1
591 withholding one set of measurements. More specifically, we used the algorithm
592 providing it the following combination of measurements: TD and isothermal dilution,
593 SOA yields and isothermal dilution, and finally SOA yields and TD.

594 The use of only the TD and isothermal dilution data corresponds for all practical
595 purposes to the previous algorithm of Karnezi et al. (2014) which has been the starting
596 point of this work. In Test A1, the absence of the yield measurements led to a significant
597 deterioration of the ability of the algorithm to estimate SOA yields at all temperatures
598 and concentrations (Fig. S7). The SOA yield error of the algorithm in the 5–35 °C
599 temperature range increased from 14-24% (when all measurements are provided) to
600 approximately 100% (Table S5). The corresponding uncertainty range also increased
601 by a factor of 4-6 (Table S6). Similar results were obtained in the other tests.

602 Figure S8 shows the volatility distribution of the products, ΔH_{vap} and α_m in Test
603 A1. High discrepancies and uncertainties were observed for the estimated
604 stoichiometric coefficients (α_i), with an increase in the relative error by a factor of 3-4
605 for the 1 and $10 \mu\text{g m}^{-3}$ bins (Table S7) compared to the case when all three types of
606 measurements are used.

607 Figures S9 and S10 show the results of the algorithm for Test A1 when only the
608 SOA yields and isothermal dilution measurements are provided as inputs to the
609 algorithm. In this case the algorithm cannot constrain well the ΔH_{vap} (relative error of
610 almost 270% with respect to the true value) as a result of the missing TD measurements.
611 This led to significant increase in the MNE_T for the estimated yields when moving far
612 from the temperature of the measurements (MNE of 65% at 15 °C and 122% at 5 °C).

613 Figures S11 and S12 show the results of the algorithm for Test A1 when only
614 yield and TD measurements are provided as inputs. In this case, there was a significant
615 reduction in the error for the ΔH_{vap} respect to the previous case (from 270% to 50%),
616 but it was still much higher than the 10% error when all three types of measurements
617 were used. This led to better agreement between the true and estimated yields at lower
618 temperatures (MNE_T of 23% and $ARSD$ of 44%).

619 When comparing TD/Dilution, Yields/Dilution, and Yields/TD results, the
620 Yield/TD combination gave the best results out of the three pairs. The isothermal
621 dilution measurements are the least valuable of the three because only a relatively small
622 fraction of the SOA evaporates and therefore the information provided is relatively
623 limited and focuses on the more volatile components of the particles. Also, TD
624 measurements are important to constrain well ΔH_{vap} and allow the more accurate
625 extrapolation of the results to other temperatures. also provides information for the
626 volatility distribution of the OA. However, our results suggest that the combination of
627 the three types of measurements does need to a major improvement over either the
628 TD/Dilution approach or the Yield/TD approach.

629

630 **4.6. Sensitivity to the Upper Limit of the Sum of Product Yields**

631 The maximum sum of the VBS product yields is one of the parameters that the user of
632 the algorithm chooses. In the analysis so far a value of 1 had been selected to reduce
633 the computational cost of the algorithm. Selected tests were repeated using a maximum
634 sum of 2 to quantify the effects of this choice on the estimated parameters and more
635 importantly on the SOA yields predicted by the parameterization. For a 4-product
636 system there are 9,191 product yield combinations and considering the discretization of
637 ΔH_{vap} and α_m , this leads to a total of 367,120 simulations (Table S3).

638 The increase in the upper limit of the sum of the yields led to an increase in the
639 “good” solutions in Tests A1, A4, B1, B2, and C2. The additional solutions had
640 different yields mostly in the $10^3 \mu\text{g m}^{-3}$ bin. This led to an increase of the mass yield

641 of this bin by 37% in Test A1, 47% in Test B1, and 29% in Test C2 (Table S8). The
642 uncertainties were even higher showing once again the difficulty to constrain the IVOC
643 range where there are no SOA measurements at very high SOA concentrations. The
644 new parametrizations had a minor effect on the estimated yields at different
645 temperatures with maximum change in the MNE_T found at 5 °C (change of 1.8% in Test
646 A1 and 1.2% in Test B2) and much smaller otherwise (Table S9). Therefore, the use of
647 the higher upper limit has an effect on the estimate of the $10^3 \mu\text{g m}^{-3}$ bin which is quite
648 uncertain in all cases, but has a minor effect on the predicted SOA yields at ambient
649 conditions.

650

651 **5. Conclusions**

652 An algorithm was developed to estimate VBS parameters for SOA formation
653 combining yield measurements from atmospheric simulation chambers with
654 thermodenuder and isothermal dilution measurements chambers. An additional feature
655 of this approach is that the algorithm estimates the uncertainty of the predicted SOA
656 yields for different SOA concentrations and temperatures, assisting in this way in the
657 design of future experiments.

658 The algorithm was evaluated against pseudo-experimental data for SOA
659 systems with known properties. The algorithm performed quite well at reproducing the
660 SOA yields at atmospherically relevant concentrations and temperatures with errors
661 less than 20% for practically all cases. This was the case even at temperatures as low
662 as 5 °C and also when the volatility range used for the parameter estimation was
663 narrower than that of the simulated SOA system. One should note that this error was
664 quite similar in most cases to the experimental error assumed in the construction of the
665 “measurement” datasets.

666 The errors in the retrieved SOA volatility distributions were in general higher
667 than those of the SOA yields. This is due to a large extent to the existence of multiple
668 solutions that can result in similar yields. The accuracy of the estimated mass fractions
669 of the more volatile SOA components improved when an additional yield measurement
670 at high SOA (e.g., at $200 \mu\text{g m}^{-3}$). The addition of this measurement also improved the
671 estimated yields at low temperatures. This therefore suggests that data points at high
672 SOA concentrations should also be obtained experimentally, together with the data
673 points at atmospherically relevant atmospheric SOA levels.

674 In all cases the algorithm results in good estimates of the effective evaporation
675 enthalpy. On the other hand, the estimates of the effective accommodation coefficient
676 are usually quite uncertain. The effect of the mass accommodation coefficient on the
677 measured quantities is relatively small compared to the other parameters (volatility
678 distribution, effective evaporation enthalpy) making it difficult to constrain. This
679 conclusion is consistent with the results of Karnezi et al. (2021). The addition of the
680 SOA yields to the inputs does not make much of a difference, because these are not
681 affected by the accommodation coefficient.

682 The approach combining yield, TD (thermograms), and isothermal dilution
683 (areograms) measurements is recommended for future parametrizations of SOA
684 formation. The use of the results of these experiments that have been designed for the
685 measurement of SOA yields to other applications (e.g., new particle formation) should
686 be performed with caution. Our results indicate that the derived parameterizations are
687 able to predict the SOA yields under different atmospheric conditions with errors of
688 around 20% or less, but the derived volatility distributions can be quite uncertain. These
689 uncertainties are higher for the tails of the distribution (the low volatility and the
690 intermediate volatility organic compounds). Different experiments should be probably
691 performed for the derivation of the VBS distribution if for example one is interested in
692 new particle formation and therefore the low volatility organics focusing on low SOA
693 concentration levels and the least volatile SOA components.

694

695

696 **6. Code and data availability**

697 The code and simulation results are available upon request
698 (spyros@chemeng.upatras.gr).

699

700 **7. Supplementary information**

701

702 **8. Author contribution**

703 PU, and SNP designed the research. PU developed the final model code. AD developed
704 a first version of the code and performed preliminary feasibility tests. DS and SNP
705 designed the experiments for the α -humulene ozonolysis and DS carried them out. PU
706 performed the simulations, the formal analysis, and wrote the original draft. Paper
707 review and editing was performed by SNP.

708

709 **9. Competing interests**

710 The authors declare that they have no conflict of interest.

711

712 **10. Financial support**

713 This work has been supported by the Chemical evolution of gas and particulate-phase
714 organic pollutants in the atmosphere (CHEVOPIN) Project of the Hellenic Foundation
715 for Research and Innovation (HFRI) under grant agreement no. 1819 and the European
716 Union's Horizon 2020 research and innovation program through the EUROCHAMP-
717 2020 Infrastructure Activity under grant agreement no. 730997.

718

719 **11. References**

720 An, W. J., Pathak, R. K., Lee, B. H. and Pandis, S. N.: Aerosol volatility measurement
721 using an improved thermodenuder: Application to secondary organic aerosol, *J.*
722 *Aerosol Sci.*, 38, 305–314, doi:10.1016/j.jaerosci.2006.12.002, 2007.

723 Baltensperger, U., Kalberer, M., Dommen, J., Paulsen, D., Alfarra, M. R., Coe, H.,
724 Fisseha, R., Gascho, A., Gysel, M., Nyeki, S., Sax, M., Steinbacher, M., Prevot, A.
725 S. H., Sjögren, S., Weingartner, E. and Zenobi, R.: Secondary organic aerosols from
726 anthropogenic and biogenic precursors, *Faraday Discuss.*, 130, 265–278,
727 doi:10.1039/b417367h, 2005.

728 Burtscher, H., Baltensperger, U., Bukowiecki, N., Cohn, P., Hüglin, C., Mohr, M.,
729 Matter, U., Nyeki, S., Schmatloch, V., Streit, N. and Weingartner, E.: Separation of
730 volatile and non-volatile aerosol fractions by thermodesorption: Instrumental
731 development and applications, *J. Aerosol Sci.*, 32, 427–442, doi:10.1016/S0021-
732 8502(00)00089-6, 2001.

733 Cain, K. P., Karnezi, E. and Pandis, S. N.: Challenges in determining atmospheric
734 organic aerosol volatility distributions using thermal evaporation techniques,
735 *Aerosol Sci. Technol.*, 54, 941–957, doi:10.1080/02786826.2020.1748172, 2020.

736 Cappa, C. D.: A model of aerosol evaporation kinetics in a thermodenuder, *Atmos.*
737 *Meas. Tech.*, 3, 579–592, doi:10.5194/amt-3-579-2010, 2010.

738 Cappa, C. D. and Jimenez, J. L.: Quantitative estimates of the volatility of ambient
739 organic aerosol, *Atmos. Chem. Phys.*, 10, 5409–5424, doi:10.5194/acp-10-5409-
740 2010, 2010.

741 Donahue, N. M., Robinson, A. L., Stanier, C. O. and Pandis, S. N.: Coupled
742 partitioning, dilution, and chemical aging of semivolatile organics, *Environ. Sci.*
743 *Technol.*, 40, 2635–2643, doi:10.1021/es052297c, 2006.

744 Emery, C., Liu, Z., Russell, A. G., Odman, M. T., Yarwood, G., and Kumar, N.:
745 Recommendations on statistics and benchmarks to assess photochemical model
746 performance, *J. Air Waste Manag. Assoc.*, 67, 582–598,
747 doi:10.1080/10962247.2016.1265027, 2017.

748 Epstein, S. A., Riipinen, I. and Donahue, N. M.: A semiempirical correlation between
749 enthalpy of vaporization and saturation concentration for organic aerosol, *Environ.*
750 *Sci. Technol.*, 44, 743–748, doi:10.1021/es902497z, 2010.

751 Fuchs, N. A. and Sutugin, A. G.: *Highly Dispersed Aerosols*, Ann Arbor Science
752 Publishers, Ann Arbor, London., 1970.

753 Fuentes, E. and McFiggans, G.: A modeling approach to evaluate the uncertainty in
754 estimating the evaporation behaviour and volatility of organic aerosols, *Atmos.*
755 *Meas. Tech.*, 5, 735–757, doi:10.5194/amt-5-735-2012, 2012.

756 Gao, L., Song, J., Mohr, C., Huang, W., Vallon, M., Jiang, F., Leisner, T., and Saathoff,
757 H.: Kinetics, SOA yields, and chemical composition of secondary organic aerosol
758 from β -caryophyllene ozonolysis with and without nitrogen oxides between 213
759 and 313 K, *Atmos. Chem. Phys.*, 22, 6001–6020, doi:10.5194/acp-22-6001-2022,
760 2022

761 Grieshop, A. P., Miracolo, M. A., Donahue, N. M. and Robinson, A. L.: Constraining
762 the volatility distribution and gas-particle partitioning of combustion aerosols using
763 isothermal dilution and thermodenuder measurements, *Environ. Sci. Technol.*, 43,
764 4750–4756, doi:10.1021/es8032378, 2009.

765 Huffman, J. A., Docherty, K. S., Mohr, C., Cubison, M. J., Ulbrich, I. M., Ziemann, P.
766 J., Onasch, T. B. and Jimenez, J. L.: Chemically-resolved volatility measurements
767 of organic aerosol from different sources, *Environ. Sci. Technol.*, 43, 5351–5357,
768 doi:10.1021/es803539d, 2009.

769 IPCC: *Climate Change 2021: The Physical Science Basis. Contribution of Working*
770 *Group I to the Sixth Assessment Report of the Intergovernmental Panel on Climate*
771 *Change*, Cambridge University Press, Cambridge, United Kingdom,
772 doi:10.1017/9781009157896, 2021.

773 Kalberer, M., Paulsen, D., Sax, M., Steinbacher, M., Dommen, J., Prevot, A. S. H.,
774 Fisseha, R., Weingartner, E., Frankevich, V., Zenobi, R. and Baltensperger, U.:

775 Identification of polymers as major components of atmospheric organic aerosols,
776 Science, 303, 1659–1662, doi:10.1126/science.1092185, 2004.

777 Kanakidou, M., Seinfeld, J. H., Pandis, S. N., Barnes, I., Dentener, F. J., Facchini, M.
778 C., Van Dingenen, R., Ervens, B., Nenes, A., Nielsen, C. J., Swietlicki, E., Putaud,
779 J. P., Balkanski, Y., Fuzzi, S., Horth, J., Moortgat, G. K., Winterhalter, R., Myhre,
780 C. E. L., Tsigaridis, K., Vignati, E., Stephanou, E. G. and Wilson, J.: Organic
781 aerosol and global climate modelling: A review, Atmos. Chem. Phys., 5, 1053–
782 1123, doi:10.5194/acp-5-1053-2005, 2005.

783 Karnezi, E., Riipinen, I. and Pandis, S. N.: Measuring the atmospheric organic aerosol
784 volatility distribution: A theoretical analysis, Atmos. Meas. Tech., 7, 2953–2965,
785 doi:10.5194/amt-7-2953-2014, 2014.

786 Lane, T. E., Donahue, N. M. and Pandis, S. N.: Effect of NO_x on secondary organic
787 aerosol concentrations, Environ. Sci. Technol., 42, 6022–6027,
788 doi:10.1021/es703225a, 2008.

789 Lee, B. H., Kostenidou, E., Hildebrandt, L., Riipinen, I., Engelhart, G. J., Mohr, C.,
790 Decarlo, P. F., Mihalopoulos, N., Prevot, A. S. H., Baltensperger, U. and Pandis, S.
791 N.: Measurement of the ambient organic aerosol volatility distribution: Application
792 during the Finokalia Aerosol Measurement Experiment (FAME-2008), Atmos.
793 Chem. Phys., 10, 12149–12160, doi:10.5194/acp-10-12149-2010, 2010.

794 Lee, B. H., Pierce, J. R., Engelhart, G. J. and Pandis, S. N.: Volatility of secondary
795 organic aerosol from the ozonolysis of monoterpenes, Atmos. Environ., 45, 2443–
796 2452, doi:10.1016/j.atmosenv.2011.02.004, 2011.

797 Lim, S. S., Vos, T., Flaxman, A. D., Danaei, G., Shibuya, K., Adair-Rohani, H., Amann,
798 M., Anderson, H. R., Andrews, K. G., Aryee, M., Atkinson, C., Bacchus, L. J.,
799 Bahalim, A. N., Balakrishnan, K., Balmes, J., Barker-Collo, S., Baxter, A., Bell, M.
800 L., Blore, J. D., Blyth, F., Bonner, C., Borges, G., Bourne, R., Boussinesq, M.,
801 Brauer, M., Brooks, P., Bruce, N. G., Brunekreef, B., Bryan-Hancock, C., Bucello,
802 C., Buchbinder, R., Bull, F., Burnett, R. T., Byers, T. E., Calabria, B., Carapetis, J.,
803 Carnahan, E., Chafe, Z., Charlson, F., Chen, H., Chen, J. S., Cheng, A. T. A., Child,
804 J. C., Cohen, A., Colson, K. E., Cowie, B. C., Darby, S., Darling, S., Davis, A.,
805 Degenhardt, L., Dentener, F., Des Jarlais, D. C., Devries, K., Dherani, M., Ding, E.
806 L., Dorsey, E. R., Driscoll, T., Edmond, K., Ali, S. E., Engell, R. E., Erwin, P. J.,
807 Fahimi, S., Falder, G., Farzadfar, F., Ferrari, A., Finucane, M. M., Flaxman, S.,
808 Fowkes, F. G. R., Freedman, G., Freeman, M. K., Gakidou, E., Ghosh, S.,

809 Giovannucci, E., Gmel, G., Graham, K., Grainger, R., Grant, B., Gunnell, D.,
810 Gutierrez, H. R., Hall, W., Hoek, H. W., Hogan, A., Hosgood, H. D., Hoy, D., Hu,
811 H., Hubbell, B. J., Hutchings, S. J., Ibeanusi, S. E., Jacklyn, G. L., Jasrasaria, R.,
812 Jonas, J. B., Kan, H., Kanis, J. A., Kassebaum, N., Kawakami, N., Khang, Y. H.,
813 Khatibzadeh, S., Khoo, J. P., Kok, C., et al.: A comparative risk assessment of
814 burden of disease and injury attributable to 67 risk factors and risk factor clusters
815 in 21 regions, 1990-2010: A systematic analysis for the Global Burden of Disease
816 Study 2010, *Lancet*, 380, 2224–2260, doi:10.1016/S0140-6736(12)61766-8, 2012.

817 Louvaris, E. E., Florou, K., Karnezi, E., Papanastasiou, D. K., Gkatzelis, G. I. and
818 Pandis, S. N.: Volatility of source apportioned wintertime organic aerosol in the
819 city of Athens, *Atmos. Environ.*, 158, 138–147, doi:10.1016/j.atmosenv.2017.
820 03.042, 2017a.

821 Louvaris, E. E., Karnezi, E., Kostenidou, E., Kaltsonoudis, C. and Pandis, S. N.:
822 Estimation of the volatility distribution of organic aerosol combining
823 thermodenuder and isothermal dilution measurements, *Atmos. Meas. Tech.*, 10,
824 3909–3918, doi:10.5194/amt-10-3909-2017, 2017b.

825 Odum, J. R., Hoffmann, T., Bowman, F., Collins, D., Flagan, R. C. and Seinfeld, J. H.:
826 Gas/particle partitioning and secondary organic aerosol yields, *Environ. Sci.*
827 *Technol.*, 30, 2580–2585, doi:10.1021/es950943+, 1996.

828 Pankow, J. F.: An absorption model of gas/particle partitioning of organic compounds
829 in the atmosphere, *Atmos. Environ.*, 28, 185–188, doi:10.1016/1352-
830 2310(94)90093-0, 1994a.

831 Pankow, J. F.: An absorption model of the gas/aerosol partitioning involved in the
832 formation of secondary organic aerosol, *Atmos. Environ.*, 28, 189–193,
833 doi:10.1016/1352-2310(94)90094-9, 1994b.

834 Pathak, R. K., Stanier, C. O., Donahue, N. M. and Pandis, S. N.: Ozonolysis of α -pinene
835 at atmospherically relevant concentrations: Temperature dependence of aerosol
836 mass fractions (yields), *J. Geophys. Res.*, 112, 1–8, doi:10.1029/2006JD007436,
837 2007a.

838 Pathak, R. K., Presto, A. A., Lane, T. E., Stanier, C. O., Donahue, N. M. and Pandis, S.
839 N.: Ozonolysis of α -pinene: Parameterization of secondary organic aerosol mass
840 fraction, *Atmos. Chem. Phys.*, 7, 3811–3821, doi:10.5194/acp-7-3811-2007,
841 2007b.

842 Pope, C. A. and Dockery, D. W.: Health effects of fine particulate air pollution: Lines
843 that connect, *J. Air Waste Manag. Assoc.*, 56, 709–742,
844 doi:10.1080/10473289.2006.10464485, 2006.

845 Quéléver, L. L. J., Kristensen, K., Normann Jensen, L., Rosati, B., Teiwes, R.,
846 Daellenbach, K. R., Peräkylä, O., Roldin, P., Bossi, R., Pedersen, H. B., Glasius,
847 M., Bilde, M., and Ehn, M.: Effect of temperature on the formation of highly
848 oxygenated organic molecules (HOMs) from alpha-pinene ozonolysis, *Atmos.*
849 *Chem. Phys.*, 19, 7609–7625, doi:10.5194/acp-19-7609-2019, 2019.

850 Riipinen, I., Pierce, J. R., Donahue, N. M. and Pandis, S. N.: Equilibration time scales
851 of organic aerosol inside thermodenuders: Evaporation kinetics versus
852 thermodynamics, *Atmos. Environ.*, 44, 597–607, doi:10.1016/j.atmosenv.
853 2009.11.022, 2010.

854 Saha, P. K. and Grieshop, A. P.: Exploring divergent volatility properties from yield
855 and thermodenuder measurements of secondary organic aerosol from α -pinene
856 ozonolysis, *Environ. Sci. Technol.*, 50, 5740–5749, doi:10.1021/acs.est.6b00303,
857 2016.

858 Seinfeld, J. H. and Pandis, S. N.: *Atmospheric Chemistry and Physics: From Air*
859 *Pollution to Climate Change, Third.*, John Wiley & Sons, Hoboken, New Jersey.,
860 2016.

861 Sippial, D., Uruci, P., Kostenidou, E. and Pandis, S. N.: Formation of secondary organic
862 aerosol during the dark-ozonolysis of α -humulene, *Env. Sci. Atmos.*, doi:
863 10.1039/d2ea00181k2023.

864 Stanier, C. O., Pathak, R. K. and Pandis, S. N.: Measurements of the volatility of
865 aerosols from α -pinene ozonolysis, *Environ. Sci. Technol.*, 41, 2756–2763,
866 doi:10.1021/es0519280, 2007.

867 Stanier, C. O., Donahue, N. and Pandis, S. N.: Parameterization of secondary organic
868 aerosol mass fractions from smog chamber data, *Atmos. Environ.*, 42, 2276–2299,
869 doi:10.1016/j.atmosenv.2007.12.042, 2008.

870 Stark, H., Yatavelli, R. L. N., Thompson, S. L., Kang, H., Krechmer, J. E., Kimmel, J.
871 R., Palm, B. B., Hu, W., Hayes, P. L., Day, D. A., Campuzano-Jost, P., Canagaratna,
872 M. R., Jayne, J. T., Worsnop, D. R. and Jimenez, J. L.: Impact of thermal
873 decomposition on thermal desorption instruments: Advantage of thermogram
874 analysis for quantifying volatility distributions of organic species, *Environ. Sci.*
875 *Technol.*, 51, 8491–8500, doi:10.1021/acs.est.7b00160, 2017.

876 Strader, R., Lurmann, F. and Pandis, S. N.: Evaluation of secondary organic aerosol
877 formation in winter, *Atmos. Environ.*, 33, 4849–4863, doi:10.1016/S1352-
878 2310(99)00310-6, 1999.

879 Wehner, B., Philippin, S. and Wiedensohler, A.: Design and calibration of a
880 thermodenuder with an improved heating unit to measure the size-dependent
881 volatile fraction of aerosol particles, *J. Aerosol Sci.*, 33, 1087–1093,
882 doi:10.1016/S0021-8502(02)00056-3, 2002.

883 Zhang, Q., Jimenez, J. L., Canagaratna, M. R., Allan, J. D., Coe, H., Ulbrich, I., Alfarra,
884 M. R., Takami, A., Middlebrook, A. M., Sun, Y. L., Dzepina, K., Dunlea, E.,
885 Docherty, K., DeCarlo, P. F., Salcedo, D., Onasch, T., Jayne, J. T., Miyoshi, T.,
886 Shimono, A., Hatakeyama, S., Takegawa, N., Kondo, Y., Schneider, J., Drewnick,
887 F., Borrmann, S., Weimer, S., Demerjian, K., Williams, P., Bower, K., Bahreini, R.,
888 Cottrell, L., Griffin, R. J., Rautiainen, J., Sun, J. Y., Zhang, Y. M. and Worsnop, D.
889 R.: Ubiquity and dominance of oxygenated species in organic aerosols in
890 anthropogenically-influenced Northern Hemisphere midlatitudes, *Geophys. Res.*
891 *Lett.*, 34, 1–6, doi:10.1029/2007GL029979, 2007.

892

893

894

Table 1: True and estimated volatility distribution of the products for 8 different tests. The uncertainty of the estimates ($\pm\sigma$) is also included.

TEST	ΔH_{vap} (kJ mol ⁻¹)	$\log(a_m)$	Stoichiometric Coefficients (α_i) at C_i^* ($\mu\text{g m}^{-3}$)						
			10 ⁻²	10 ⁻¹	10 ⁰	10 ¹	10 ²	10 ³	10 ⁴
True A	30	-0.30	-	-	0.070	0.038	0.179	0.300	-
A1	32.9±9.6	-0.77±0.47	-	-	0.059 ±0.022	0.071 ±0.052	0.252 ±0.130	0.255 ±0.191	-
A2	32.0±9.8	-0.72±0.45	-	-	0.062 ±0.021	0.067 ±0.053	0.286 ±0.132	-	-
A3	32.0±9.8	-0.72±0.45	-	0.000 ±0.000	0.062 ±0.021	0.067 ±0.053	0.286 ±0.132	-	-
A4	34.0±9.2	-0.70±0.46	-	-	0.062 ±0.021	0.082 ±0.050	0.191 ±0.084	0.259 ±0.198	-
True B	30	-0.30	0.001	0.012	0.037	0.088	0.099	0.250	0.800
B1	33.8±9.2	-0.95±0.21	-	-	0.052 ±0.011	0.037 ±0.039	0.374 ±0.122	0.226 ±0.176	-
B2	36.5±7.6	-0.93±0.26	-	-	0.050 ±0.000	0.051 ±0.039	0.292 ±0.103	0.234 ±0.196	-
True C	115	-2.02	0.118	0.094	0.116	0.247	-	-	-
C1	104.6±24.0	-1.74±0.97	0.126 ±0.086	0.116 ±0.090	0.154 ±0.116	0.216 ±0.126	-	-	-
C2	91.2±19.2	-2.36±0.83	-	-	0.415 ±0.099	0.143 ±0.117	0.137 ±0.113	0.115 ±0.095	-

Table 2: The *mean normalized error* (MNE) between the “measurements” and “true” values, and between the “measurements” and the model estimated values for the different tests.

Test	“Measurements” vs “True” ^a			“Measurements” vs Estimated <i>MNE_M</i> ^b		
	Yield	TD	Dilution	Yield	TD	Dilution
A1	21.2	7.6	9.4	25.0	7.0	16.69
A2	21.2	7.6	9.4	25.1	7.1	16.71
A3	21.2	7.6	9.4	25.1	7.1	16.71
A4	17.8	7.6	9.4	22.4	7.1	19.7
B1	20.5	6.9	5.6	20.6	6.0	14.7
B2	18.1	6.9	5.6	19.1	7.8	18.1
C1	8.4	11.6	1.8	6.3	12.9	3.5
C2	8.4	11.6	1.8	8.6	32.4	2.3

^a Calculated by $\frac{100}{N_o} \sum_{i=1}^{N_o} \frac{|O_i - TR_i|}{O_i}$.

^b Calculated by Eq. (16).

Table 3: The *mean normalized error* between the “true” and estimated values (MNE_T) for the different tests.

Test	Yield				TD	Dilution
	5 °C	15 °C	25 °C	35 °C		
A1	24.4	21.0	17.3	13.8	5.5	19.0
A2	21.4	19.5	16.9	14.1	4.7	18.5
A3	21.4	19.5	16.9	14.1	4.7	18.5
A4	20.4	18.3	15.7	12.9	6.0	22.5
B1	31.3	21.7	13.9	8.7	4.0	13.3
B2	24.4	15.6	9.0	6.4	2.5	18.4
C1	6.2	6.8	9.6	15.5	4.4 (110 °C)* 10.6 (140 °C)*	2.7
C2	18.1	9.6	7.2	11.5	9.0 (110 °C)* 27.8 (140 °C)*	3.4

* The errors for TD were calculated up to the denoted temperature in the parenthesis.

Table 4: The *average relative standard deviation* ($ARSD$) for the different tests.

Test	Yield				TD	Dilution
	5 °C	15 °C	25 °C	35 °C		
A1	34.6	29.7	26.0	24.2	21.0	23.6
A2	32.1	28.5	25.2	23.3	21.1	23.2
A3	32.1	28.5	25.2	23.3	21.1	23.2
A4	30.8	27.2	24.5	23.3	21.0	22.1
B1	37.1	27.2	20.0	16.9	20.5	18.0
B2	33.8	25.0	18.5	15.7	18.0	15.9
C1	15.0	14.9	16.2	22.9	20.7*	16.5
C2	20.1	15.6	14.1	21.3	20.6*	9.8

* The $ARSD$ for the TD MFR values were calculated in the 20–120 °C temperature range.

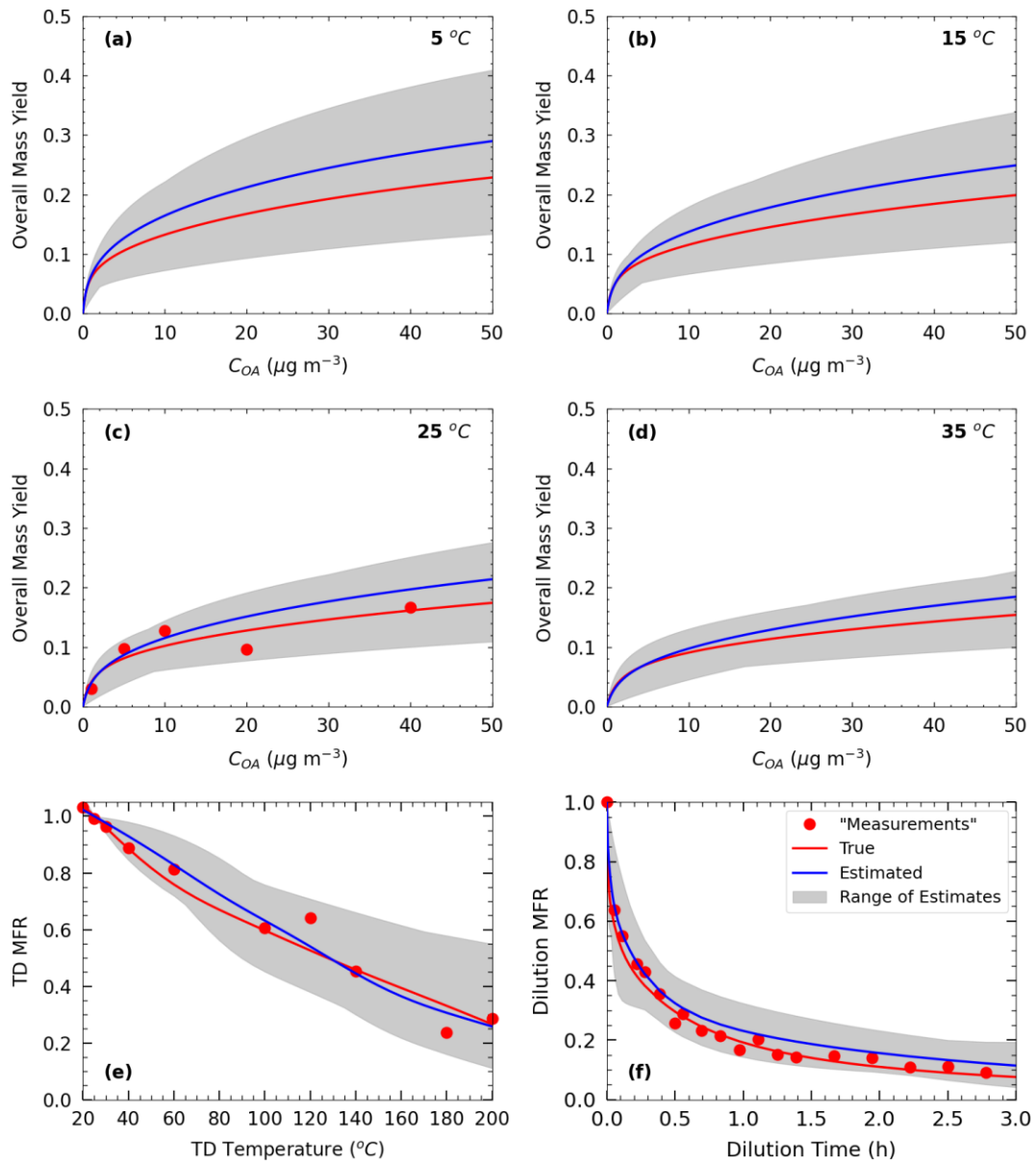


Figure 1: “Measurements” of Test A1 in Experiment A (red dots), true (red line) and estimated (blue line) yields at (a) 5 °C, (b) 15 °C, (c) 25 °C, and (d) 35 °C, (e) TD (thermogram), and (f) dilution (areogram) values. The grey area shows the range of good solutions obtained by our algorithm.

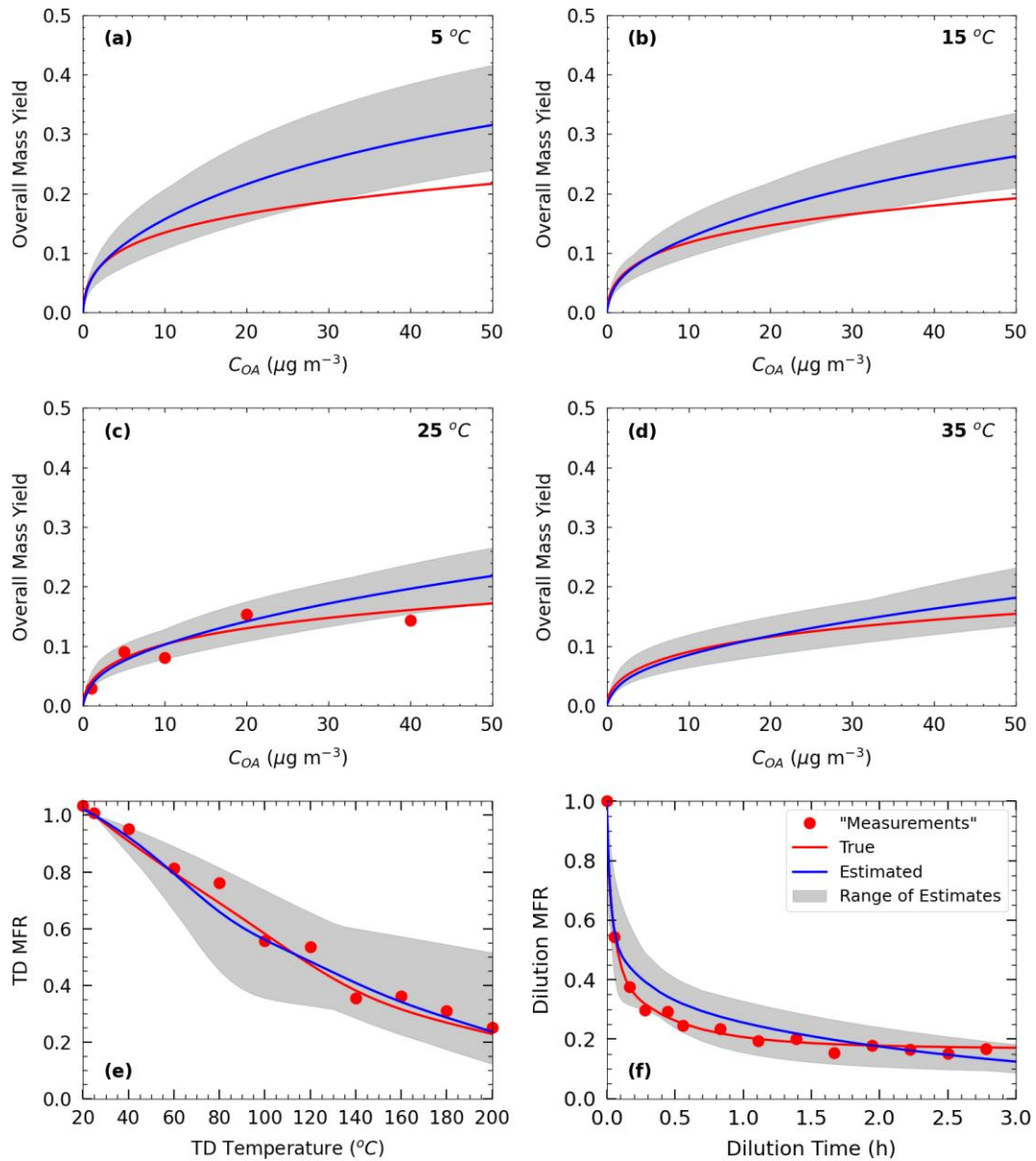


Figure 2: “Measurements” of Test B1 in Experiment B (red dots), true (red line) and estimated (blue line) yields at (a) 5 °C, (b) 15 °C, (c) 25 °C, and (d) 35 °C, (e) TD (thermogram), and (f) dilution (areogram) values. The grey area shows the range of good solutions.

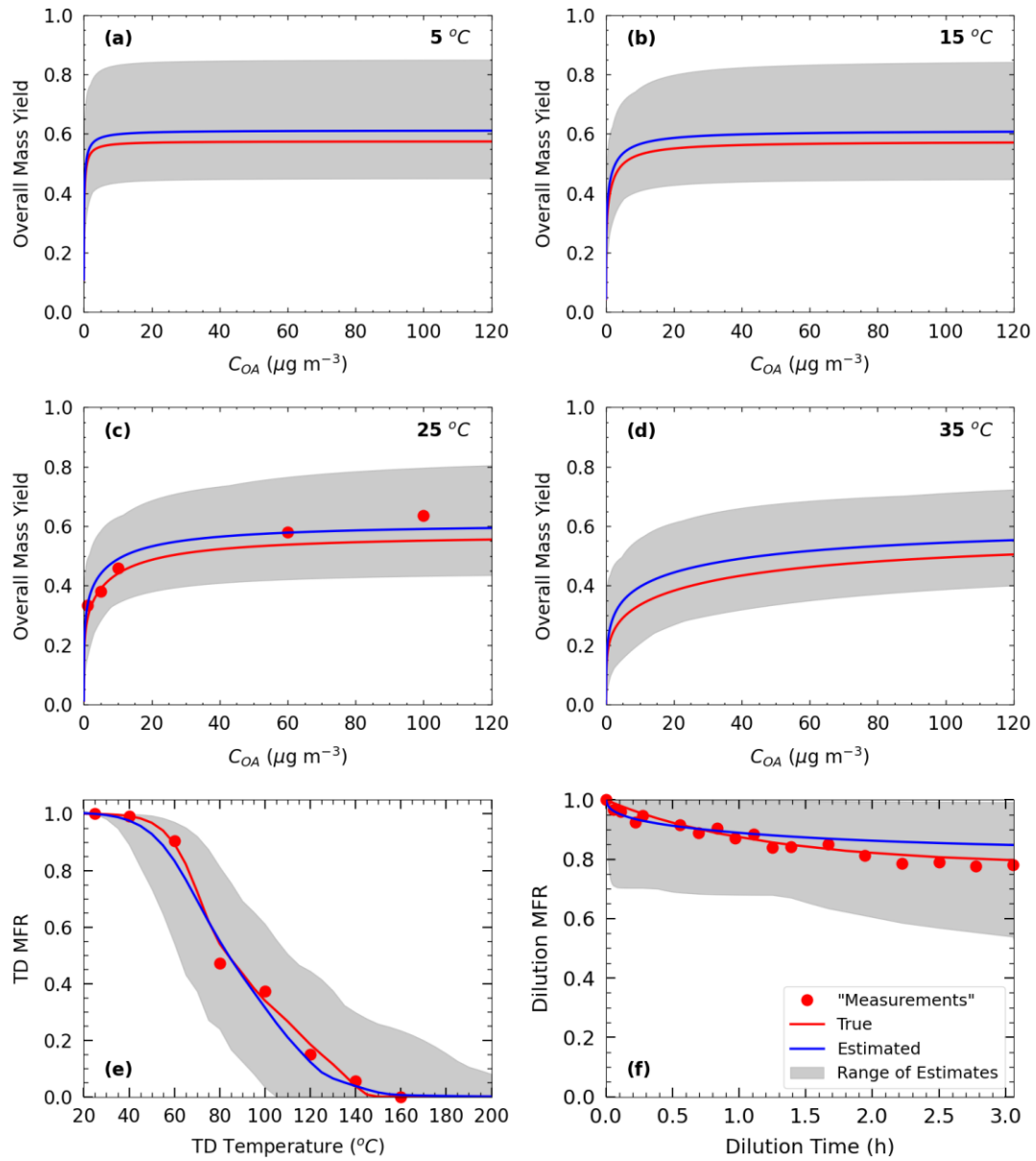


Figure 3: “Measurements” of Test C1 in Experiment C (red dots), true (red line) and estimated (blue line) yields at (a) 5 °C, (b) 15 °C, (c) 25 °C, and (d) 35 °C, (e) TD (thermogram), and (f) dilution (areogram) values. The grey area shows the range of good solutions.

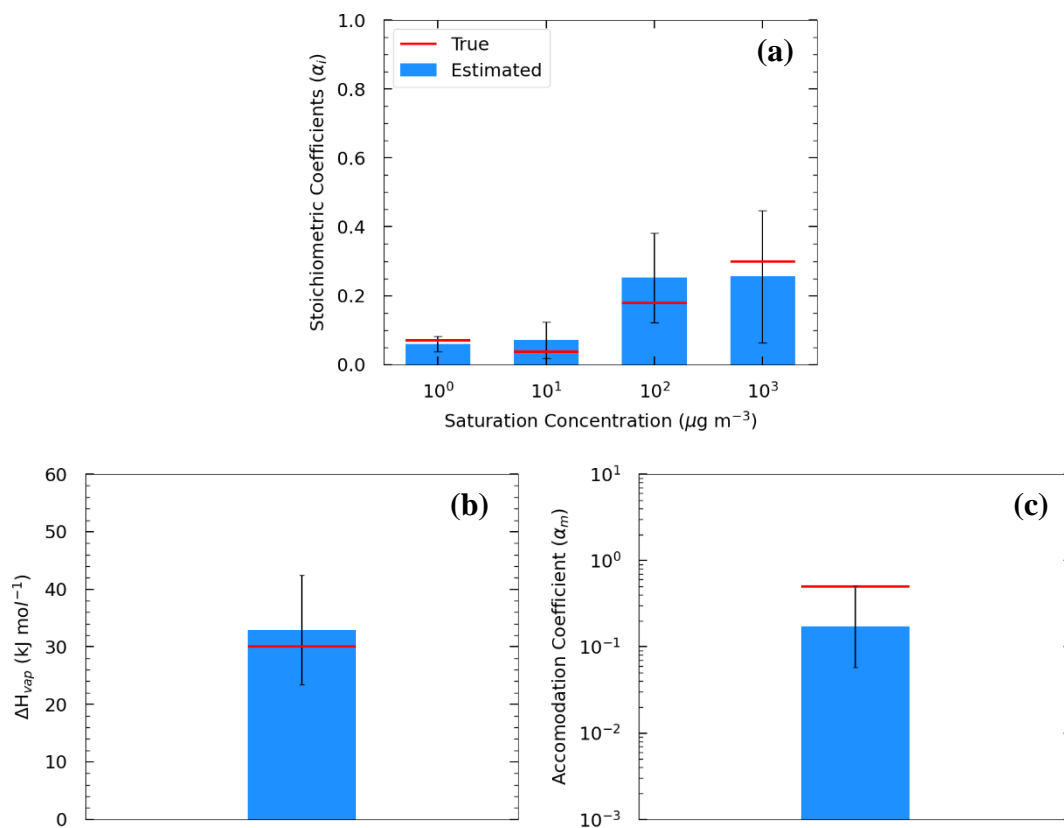


Figure 4. Estimated (bars) and true (red lines) parameter values of Experiment A in Test A1 combining yield, TD, and isothermal dilution measurements for: (a) the volatility distribution of the products, (b) ΔH_{vap} , and (c) α_m . The error bars represent the uncertainty of the estimated values.

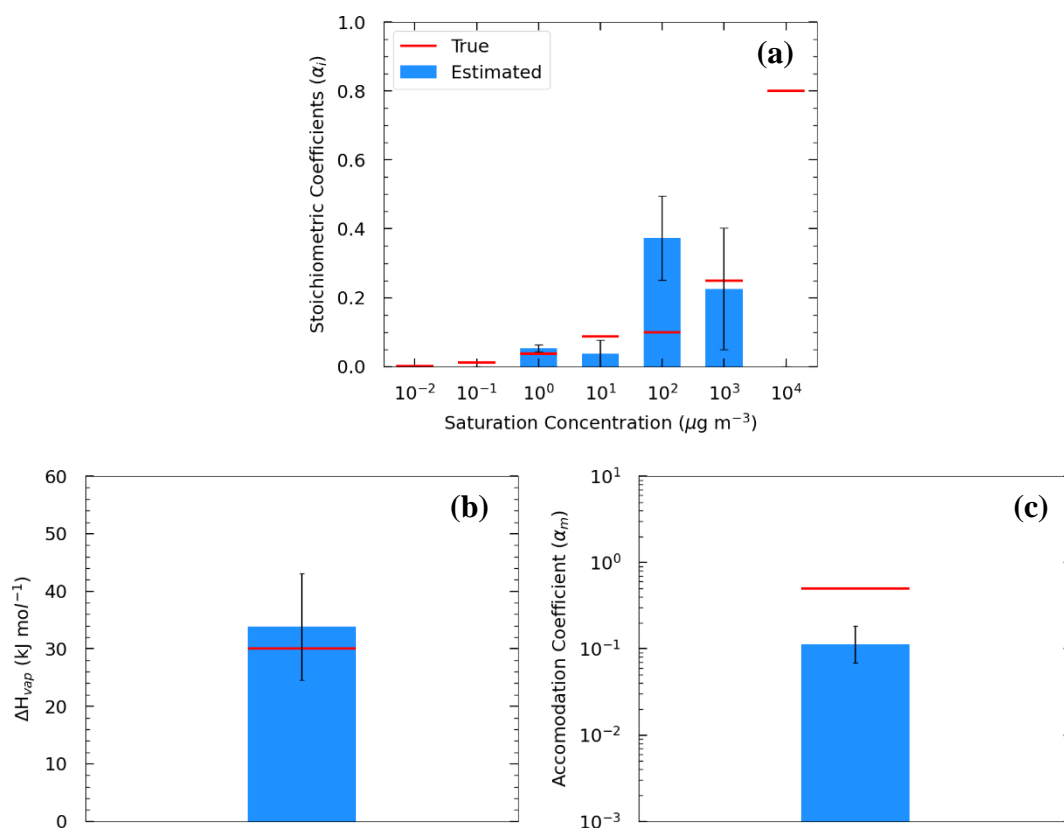


Figure 5: Estimated (bars) and true (red lines) parameter values of Experiment B in Test B1 combining yield, TD, and isothermal dilution measurements for: (a) the volatility distribution of the products, (b) ΔH_{vap} , and (c) α_m . The error bars represent the uncertainty of the estimated values.

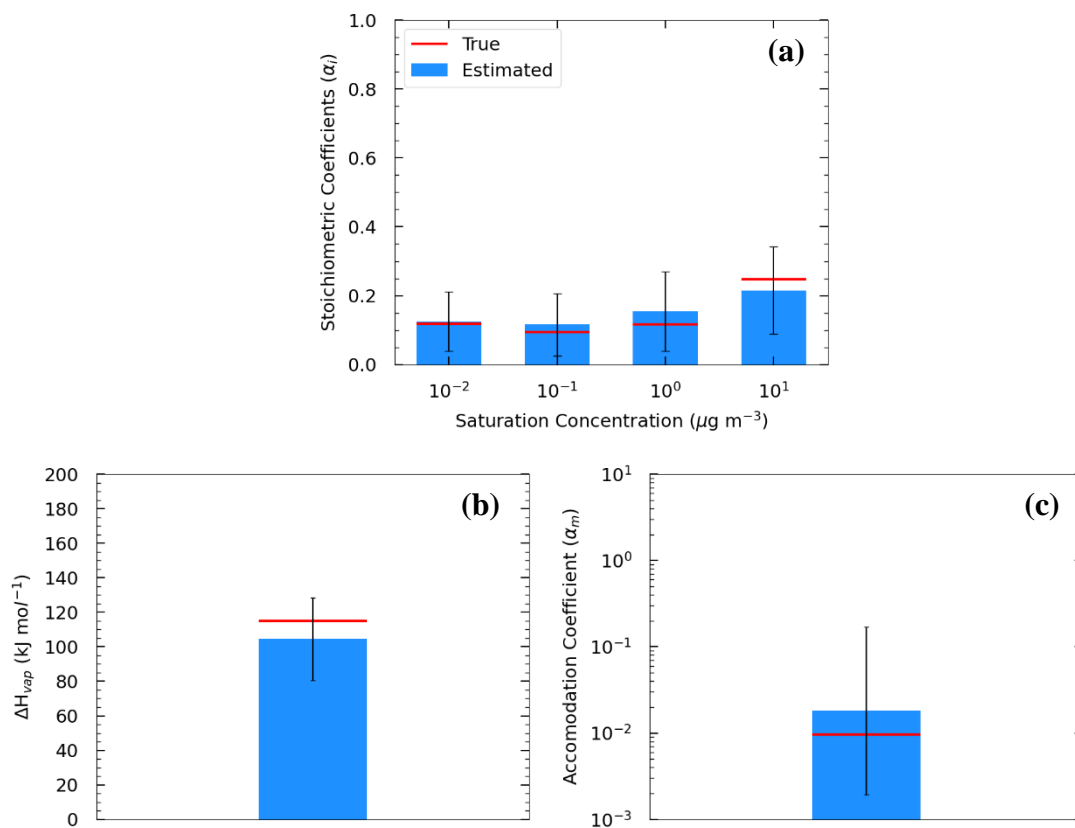


Figure 6: Estimated (bars) and true (red lines) parameter values of Experiment C in Test C1 combining yield, TD, and isothermal dilution measurements for: (a) the volatility distribution of the products, (b) ΔH_{vap} , and (c) α_m . The error bars represent the uncertainty of the estimated values.

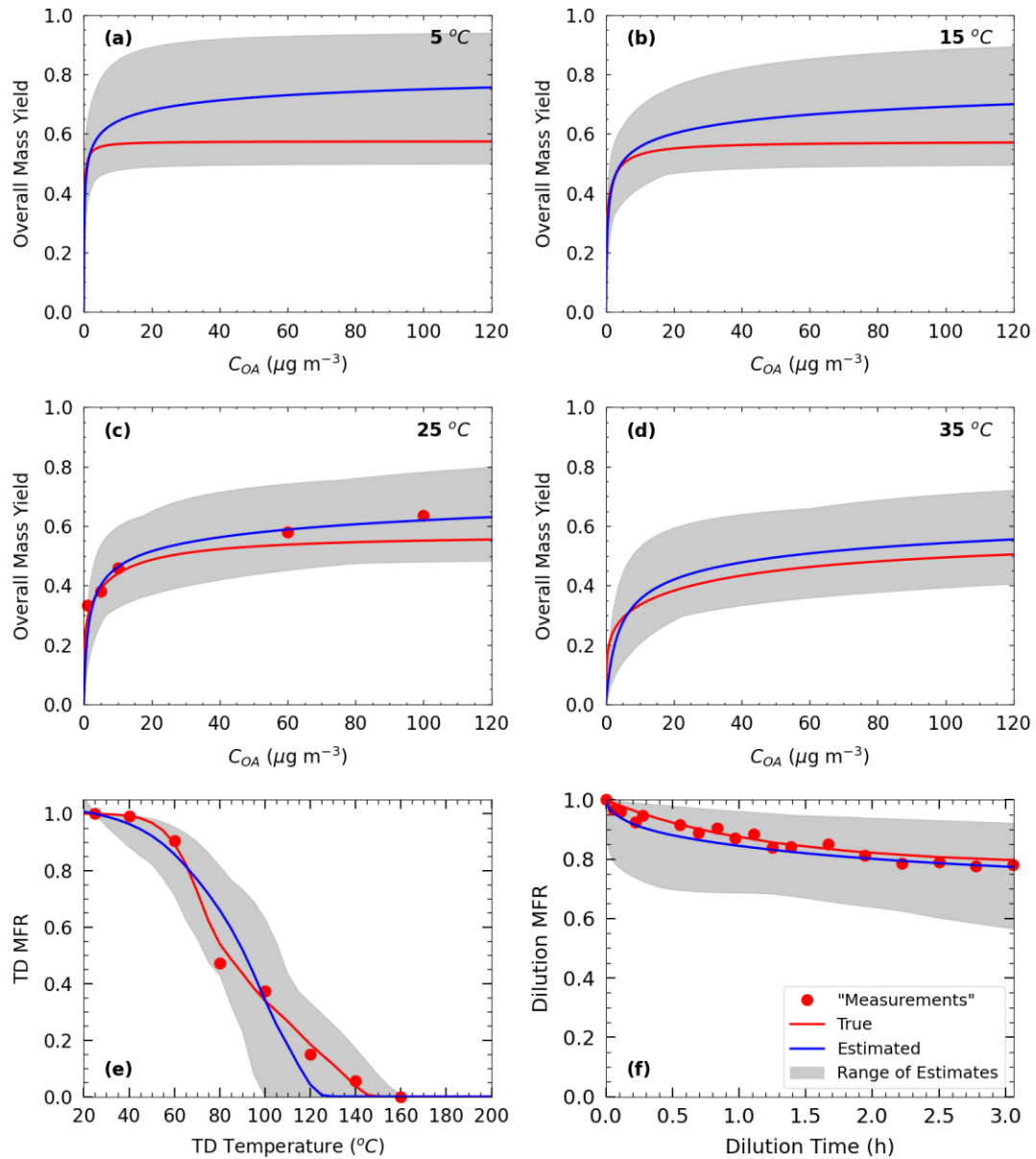


Figure 7: Yields calculated using the “true” parameters of Experiment C (red line) and the estimated (blue line) using the parameters of Test C2 for the following temperatures: (a) 5 °C, (b) 15 °C, (c) 25 °C, and (d) 35 °C. Also shown the (e) thermogram and (f) aerogram. The grey area shows the range of good solutions obtained by our algorithm.

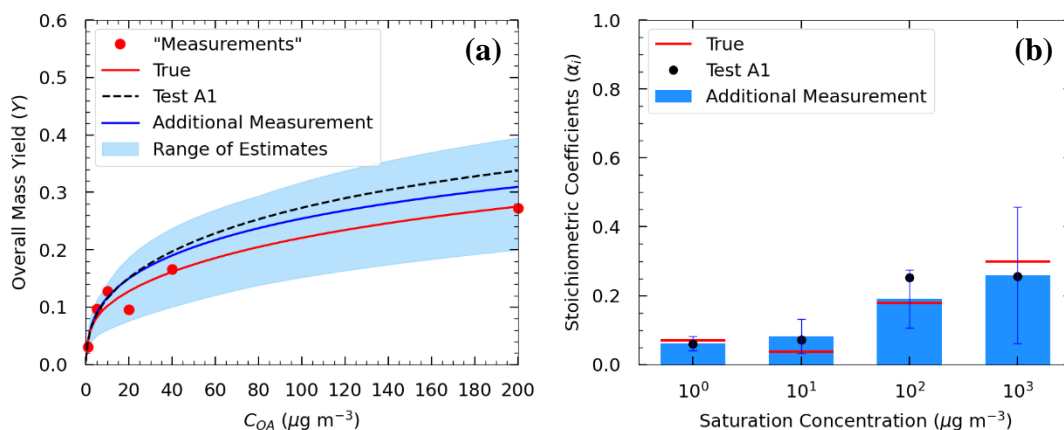


Figure 8: (a) True (red line) and estimated (blue line) yields in Test A4, and the “measurements” of Experiment A (red dots) including an additional yield “measurement” at 200 $\mu\text{g m}^{-3}$. The black dashed line corresponds to the estimated yields in Test A1. (b) Estimated volatility distribution of the products (bars) of Test A4 and the true (red lines) parameter values. The black dots correspond to the estimated volatility distribution of the products in Test A1.

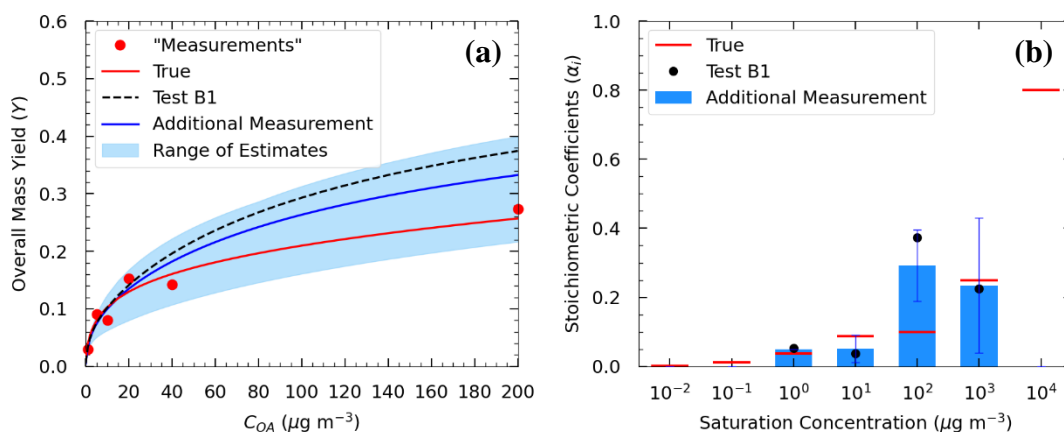


Figure 9: (a) Estimated yields (blue line) in Test B2 and “measurements” of Experiment B (red dots) including an additional yield “measurement” at 200 $\mu\text{g m}^{-3}$. The black dashed line corresponds to the estimated yields in Test B1. (b) Estimated volatility distribution of the products (bars) of Test B2 and the true (red lines) parameter values. The black dots correspond to the estimated volatility distribution of the products in Test B1.

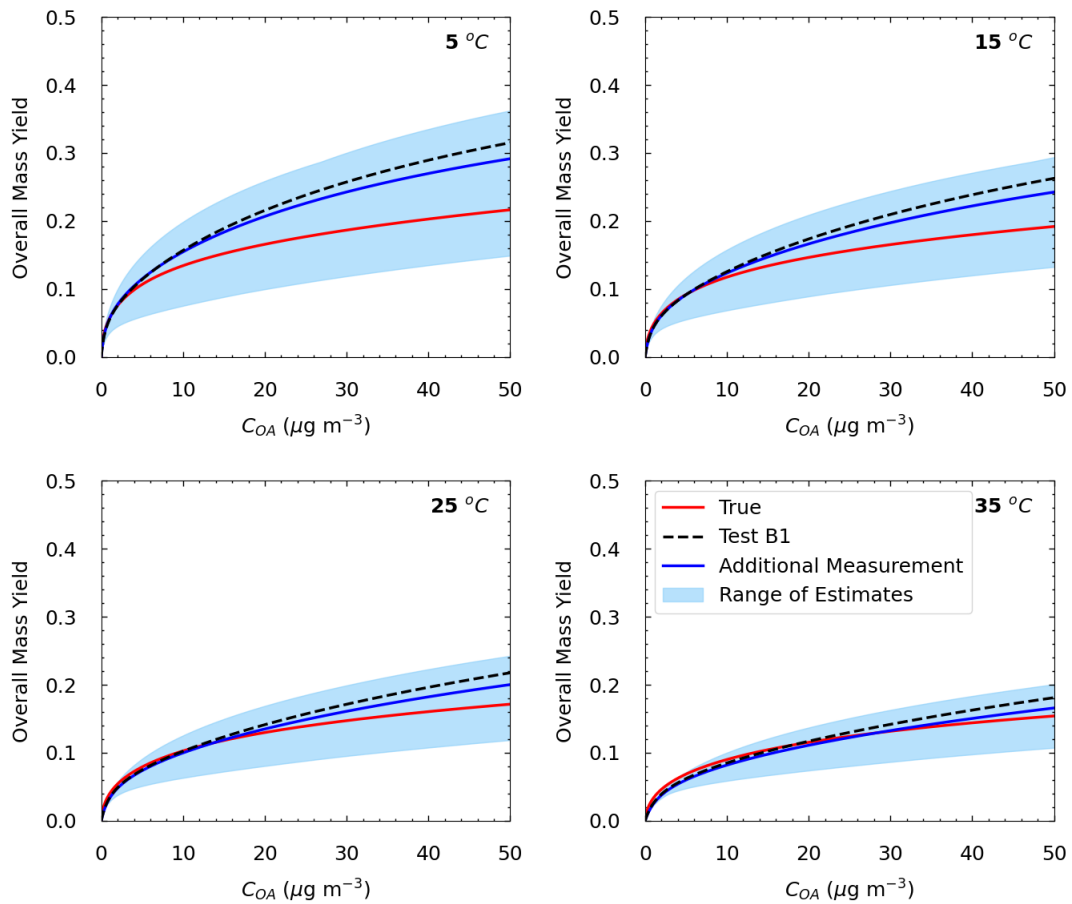


Figure 10: Yields calculated using the “true” parameters of Experiment B (red line) and the estimated (blue line) using the parameters of Test B2 for the following temperatures: 5 °C, 15 °C, 25 °C, and 35 °C. The blue area shows the range of good solutions obtained by our algorithm. The black dashed line corresponds to the estimated yields in Test B1.